Multidomain Optimization of High-Power-Density PM Electrical Machines for System Architecture Selection

Dmitry Golovanov, Luca Papini, David Gerada, Zeyuan Xu, and Chris Gerada, *Member, IEEE*

***Abstract*—The power density of electrical machines for transport applications has become a critical aspect and target of optimization. This paper looks at the development of an intelligent, rapid, flexible, and multidomain tool to aid for system-level optimization of electrical machines within next-generation high power density applications. The electromagnetic, thermal, and mechanical aspects are wholly integrated, thus enabling the optimization including the nonactive mass. The implementation and overall architecture of the tool are described, and using a case study drawn from the aerospace industry, the tool is used to compare the power density of various surface permanent magnet topologies including single airgap and dual airgap machines, highlighting the particular suitability of the dual rotor topology in achieving the best power to mass ratio. Finally, the accuracy of the tool is highlighted by practical realization and experimental validation.**

***Index Terms*—High power density, multidomain, optimization, permanent magnet machines, transportation.**

I. Introduction

With the globally increasingly stringent emissions legislations and fuel economy requirements, companies in the transportation sector are actively and intensely researching new technologies, which often involve electrification and hence, the use of electrical machines for either motoring or generation. The performance targets in this type of work are various and depend a lot on the specific industry and application. For example, "high power density" is often a key phrase to distinguish new developments. In the land transportation industry, more specifically for road transportation, where volume is often highly constrained, the key power density metric is the power to volume ratio or kW/L, with numbers such as 4.8 and 4.2 kW/L achieved by Toyota and Nissan [1], respectively. Current hybrid vehicle research programs are targeting in excess of 6 kW/L for the 2020 electrical machine challenge proposed by the U.S. Department of Energy [2], [3]. On the other hand, for the aerospace industry, mass minimization, rather than volume, is critical and the key power density metric is the power to mass ratio or kW/kg, with various numbers published to show achievements of particular developments, such as a recent 5.2 kW/kg by Siemens for a light electric aircraft [4]. Fig. 1 shows two often cited recent developments within the automotive and aerospace industries which present new points of reference for the current state of the art.

Fig. 1. State-of-the-art high power density motors in the automotive *Nissan* and aerospace industries *Siemens*.

Engineers working on the system concept and integration of the aforementioned more electric transport architectures often face a bottleneck when it comes to the electrical machine. Whilst comprehensive libraries of say, high speed bearings, or high speed turbines are normally available either through supplier input or in-house designs, for the high-performance electrical machines targeted in such work, the available data is very limited. Doing machine sizing in a manual manner for the range of options which the system architects want to investigate is too much time consuming and impractical due to the number of permutations involved, while narrowing down the options risks in missing the system optima altogether. From the foregoing discussion, clearly a tool is required to rapidly generate and assess optimal electrical machine solutions based on defined constraints taking into account the various sciences involved.

This paper describes the development of such a tool. In the first part the methodology, behind the tool development and its implementation are described. The tool is then adopted and used for an aerospace application where it is required to compare the achievable kW/kg for various permanent magnet (PM) machine configurations under an intense cooling regime, with the intent

Manuscript received March 3, 2017; revised June 20, 2017 and September 7, 2017; accepted September 13, 2017. *(Corresponding author: Luca Papini.)*

D. Golovanov, L. Papini, and D. Gerada are with the University of Nottingham, Nottingham NG7 2RD, U.K (e-mail: Dmitry.Golovanov@nottingham.ac.uk; eexlp4@nottingham.ac.uk; david.gerada@nottingham.ac.uk).

Z. Xu is with the Department of Mechanical, University of Nottingham, Nottingham NG7 2RD, U.K (e-mail: Zeyuan.Xu@nottingham.ac.uk).

C. Gerada is with the School of Electrical and Electronic Engineering, University of Nottingham, Nottingham NG7 2RD, U.K (e-mail: chris.gerada@nottingham.ac.uk).

Color versions of one or more of the figures in this paper are available online at http://ieeexplore.ieee.org.

Digital Object Identifier 10.1109/TIE.2017.2772188

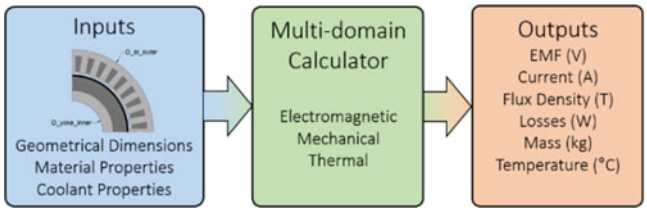

Fig. 2. Multidomain calculators required for optimization.

of establishing, which PM machine topology yields the best power to mass characteristic.

II. Requirement and Methodology

At the early stages of transport electrification projects, the known data with which the system architects start is typically quite limited in nature. This often includes fundamental items, such as the power rating based on the vehicle size, a speed range based on existing turbines or engine designs, together with a list of available coolants. For the example in hand, the power node investigated of 1 MW has to be achieved at a single speed only, and a family of existing turbines within speeds from 8000 to 20 000 rpm are available. While the overall goal of maximizing the kW/kg is known, other items such as the volume, or aspect ratio of the machine are not specified and can be accommodated by the system designers who are often starting from a blank (flexible) design space.

Surface permanent magnet (SPM) machines are known to be capable of achieving the highest power-densities [5] for a single power-speed design point requirement. However, various types of SPM machines exist (inner rotor (IR), outer rotor (OR), dual-airgap, etc.) and it is not immediately obvious which of the aforesaid SPM configurations gives the best kW/kg if the volume is left unconstrained.

Finally, in determining which type of SPM machine yields the best kW/kg, therefore, targeting mass minimization, it is important that the inactive mass is considered within the optimization procedure. By way of example, considering a previously developed high power density aerospace motor, the inactive mass is as high as 34% of the total machine mass [6]. In many classical optimization approaches, the optimization is first done on the electromagnetics, then a housing is designed around the optimized electromagnetic design. However, the housing can be a very significant proportion of the total mass and integrating the housing design with the overall machine kW/kg optimization has high potential for extra power density entitlement.

Appropriate multidomain calculators, which serve as the essential building blocks with which the kW/kg optimization is performed, are required. To this end, for each SPM topology considered, electromagnetic, thermal, and mechanical analytical models are developed, as shown in Fig. 2.

The arbitrary SPM machines are defined in terms of their characterising geometries, constituent materials defined by their magnetic, mechanical and thermal properties, as well as the coolant properties which include the coolant temperature and flow rate. The following sections detail the multidomain calculators implemented and used within the optimization tool.

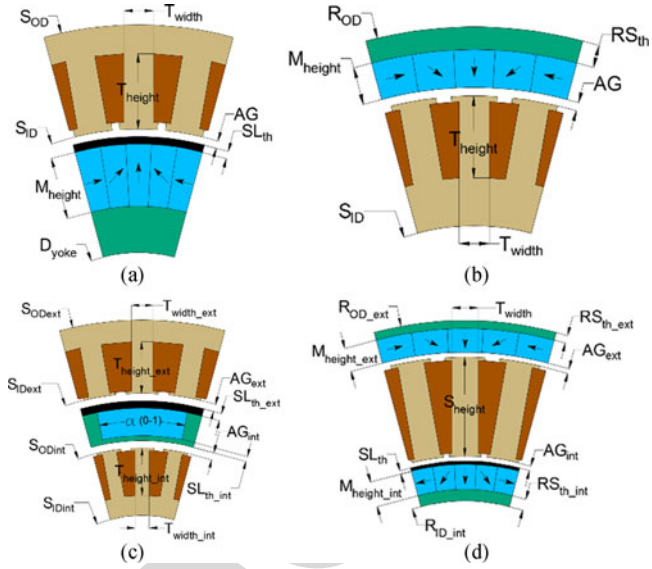

Fig. 3. Considered topologies of PM machines. (a) IR. (b) OR (c) DS. (d) DR.

III. Electromagnetic Calculator

The analytical electromagnetic calculations are performed on any arbitrary geometry defined for the topologies under investigation. The geometrical parameters of the considered machine topologies are shown in Fig. 3, which include single air gap machines, namely the IR and the OR topologies. Furthermore, dual air gap machines are also considered namely the dual stator (DS) and the dual rotor (DR) topologies. An ideal Halbach array structure is selected for the rotor of the IR, OR, and DR topologies, allowing to achieve high fundamental air-gap flux densities whilst reducing the harmonic content [7], and the amount of soft magnetic material required for the rotor core. The electromagnetic model for the considered topologies is for a three-phase single layer distributed winding, with an additional winding group for the (DS) machine. The material selected for the stator structure consists of multiple ultrathin cobalt–iron laminations in a thickness of 0.05 mm which represents a best-in-class material in terms of saturation flux density and high frequency core losses. The arbitrary machine geometry is initially used to compute the no-load magnetic field according to the analytical model of machines with a Halbach array [8]. Under linear behaviour of magnetic materials, the solution for the fundamental of the radial component of flux density in the air gap for the IR and OR topologies is given in [7]. The flux density estimation for the DS topology had been described in [9].

The flux density in the air gaps of the DR machine is evaluated by the introduction of auxiliary virtual PMs [10] that represent the influence of ferromagnetic teeth on the magnetic field. The phase rms value back EMF for the IR, OR, DS, and DR designs is then calculated by the following equation:

$$E_{\rm ph} = \pi\sqrt{2}\, f_e W_{\rm ph} \Phi_0 K_w \tag{1}$$

where $W_{\rm ph}$ is the number of turns per phase, f_e is the electrical fundamental frequency, K_w is the winding factor, and Φ_0 is the no load fundamental flux linkage per pole calculated by the

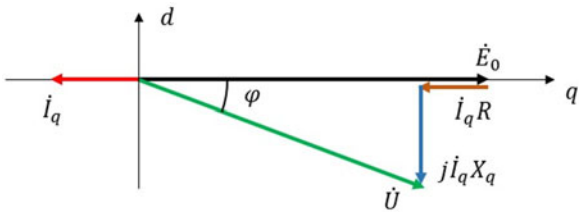

Fig. 4. Vector diagram of considered synchronous machines.

following equation:

$$\Phi_0 = \frac{\pi}{p} L\, R_{\rm st} \langle B_r \rangle . \tag{2}$$

In the above equation, $\langle B_r \rangle$ is the average value of the fundamental radial flux density component in the air gap, p is the number of rotor pole pairs, L is the active axial length, and $R_{\rm st}$ the radius of the stator surface.

The machine is analyzed in generation mode. The d–q axis model is adopted with the rotor considered aligned to the q-axis. Imposing the d-axis current to zero, the resulting phasor diagram is shown in Fig. 4. The phase current $I_{\rm ph}$ can then be estimated from the following equation:

$$\mathrm{I_{ph}} = \frac{P_{\rm el}}{m \cdot E_{\rm ph} \cdot \eta} \tag{3}$$

where $P_{\rm el}$ is the electromagnetic power, m is the number of phases, and η is the efficiency. The number of turns is limited by the fixed dc-link voltage which is set to 2 kV while the winding resistance is calculated considering a slot fill factor of 0.5. The reactance is calculated by means of analytical expressions [11], and the power factor is thus derived accordingly. For the loss calculation, the dc copper losses and the iron losses are considered.

The flux densities for the iron loss calculation are evaluated by means of a linear magnetic circuit calculation and considered as average values on the overall structure. The armature current flux density is evaluated using the approach described in [12].

Given the specific loss of a lamination material say at a frequency of 60 Hz and at an induction of 1 T—$\mathrm{W_{Fe\_60,1}}$, for any stator fundamental frequency—f_s, and iron flux-density level B_s, the specific iron losses can be approximated from [13] the following equation:

$$W_{\rm Fe} = \frac{W_{\rm Fe\_60,1}}{2} {B_s}^{1.6} \frac{f_s}{60} + \frac{W_{\rm Fe\_60,1}}{2} {B_s}^2 \left(\frac{f_s}{60}\right)^2 \tag{4}$$

where B_s is the on-load flux density [9].

IV. Mechanical Calculator

For the mechanical calculator, the input is the same arbitrary active electrical machine geometry of Fig. 3, together with the mechanical properties of the constituent materials. Based on these inputs, the mechanical calculator estimates the mass of the active materials (i.e., mass of copper, magnets, and iron) and also sizes an appropriate housing around the active geometry with the intent of calculating the nonactive mass. Fig. 5 details the housing sized around the IR SPM configuration showing the

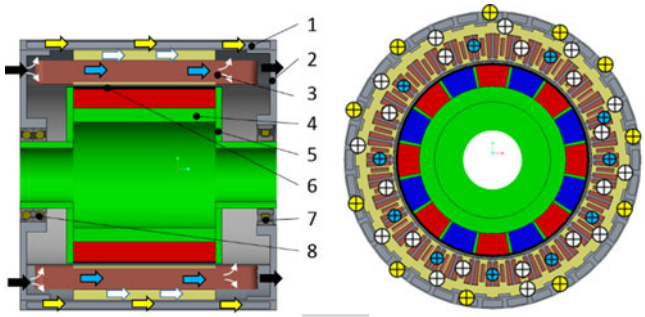

Fig. 5. General housing design and cooling configurations for IR topology.

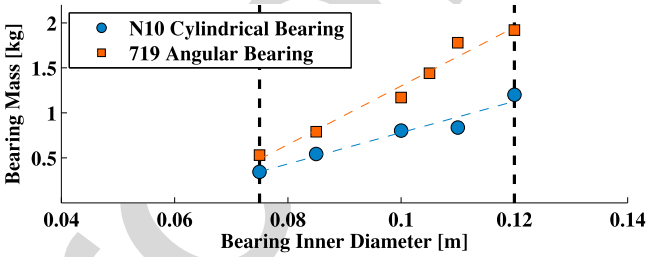

Fig. 6. Bearing mass data and interpolating functions.

TABLE I
Inner Rotor Machine Inactive Parts and Materials

Item#	Descriptions	Material	Density (kg/m^3)	Form
		Stator Housing		
1	Housing shells (inner+outer)	AL6061	2700	Cylindrical shell
2	Two end flanges	AL6061	2700	Hollow disk
3	Cooling channels	AL6061	2700	Rectangular
		Rotor Assembly		
4	Rotor shaft	17-4PH	7780	Cylindrical shaft
5	Rotor balance plates	SS316	7990	Hollow disk
6	Magnet retention sleeve	Carbon Fiber	1600	Cylindrical ring
		Bearings		
7	Drive end bearings		✗	✗
8	Non drive end bearings		✗	✗

axial cross section (*left*) and radial cross section (*right*) with the colour grey denoting the stator housing, colour green denoting the rotor shaft, colour yellow for the stator laminations, colour brown for the copper, and colour red/blue for the permanent magnets.

Continuing with the case of the IR topology, there are a total of eight inactive parts which are sized for a mechanical factor of safety of at least 1.5 and assuming the machine to be foot mounted. The aforesaid eight inactive parts are numbered in Fig. 5 and listed in Table I. The stator housing (*grey*) is made up of items#1–#3 which correspond to two cylindrical shells (item#1), enclosing end-flanges (item#2), and cooling channels. All the aforesaid components are made of lightweight aluminium having a density of 2700 kg/m^3 in order to minimize the mass.

The rotor assembly supporting the Halbach magnet array is also made up of three constituent parts, items#4–#6 correspond-

ing to a rotor shaft made of high strength, magnetically permeable 17-4ph stainless steel which has a hollow cross section to minimize the mass (item#4), two rotor balance plates made of stainless steel (item#5), and a lightweight carbon-fiber sleeve (item#6) which retains the magnet under compression. Prestress is applied within the carbon-fiber sleeve to ensure that a positive pressure is kept on the magnets throughout the operational speed range as described by the following equation:

$$P_{\text{total}} = P_{\text{prestress}} - P_{\text{mag speed}} - P_{\text{sleeve speed}} > 0 \quad (5)$$

where $P_{\text{prestress}}$ is the prestress pressure, while $P_{\text{mag speed}}$ $P_{\text{sleeve speed}}$ are the pressure of the magnet and the sleeve, respectively, due to centrifugal affects. The calculation of these depend on the speed, material density as well as the radii of the sleeve and magnet [22]

While ensuring that the condition described by (5) is satisfied, the maximum pressure applied on the sleeve should not result in the stress within the sleeve reaching values beyond the yield strength of the sleeve material as described by the following equation:

$$\sigma_{\text{total}} = \sigma_{\text{prestress}} + \sigma_{\text{sleeve speed}} < \sigma_{\text{material}} \quad (6)$$

where $\sigma_{\text{prestress}}$ is the stress due to the preload pressure, $\sigma_{\text{sleeve speed}}$ is the sleeve stress at the overspeed condition, and σ_{material} is the material yield strength.

Apart from maintaining the stress of the various components within a safe limit, in sizing the inactive parts it is also important to ensure that there is sufficient torque transmission capability. To this end a minimum shaft diameter D_{min} is calculated based on the torque transmission requirement as described by the following equation:

$$D_{\text{min}} = \frac{2 \cdot J \cdot \tau}{T} \quad (7)$$

where T is the shaft torque, and J is the hollow shaft's polar moment of inertia.

With the minimum shaft diameter determined, the bearing inner diameter can, therefore, be selected. For the drive-end, a cylindrical bearing is selected (item#7), while for the nondrive-end a pair of back-to-back angular-contact bearings are used (item#8), as shown in Fig. 5. In determining the bearing mass, linear correlations between bearing inner diameter and mass of the bearing are derived based on the available bearing data [14], as shown in Fig. 6.

The procedure for calculating the inactive mass around arbitrary geometries of the OR, DS, and DR topologies follows a similar methodology to that described for the IR and hence, does not necessitate a detailed description. The cross sections for these machines are shown in Fig. 7 with the same color coding maintained as with the IR machine.

For the OR topology, as shown in Fig. 7(a), the rotor assembly is made-up of a lightweight structure in titanium, with the magnets attached at the inside of the aforesaid structure. Titanium is used for the rotor inactive material since the large rotor diameter would result in a comparatively large inactive mass if stainless steel were to be used as with the IR topology. The DS topology structure is conceptually similar to the OR, with an external stator and stator housing added, as shown in Fig. 7(b). Finally, for the DR topology, the internal rotor assembly has a rigid connection by an end-disk to the external one. The stator core of the machine is supported by bars through the stator laminations which are fixed to a mounting plate at one end of the machine, as shown in Fig. 7(c).

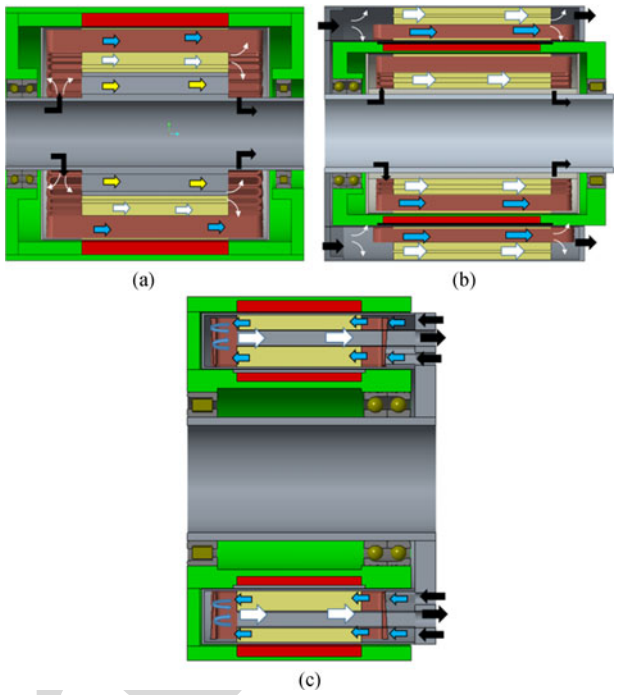

Fig. 7. General housing design and cooling configurations for OR, DS, and DR topologies. (a) Outer rotor machine design. (b) Double stator machine design. (c) Double rotor machine design.

V. Thermal Calculator

For the thermal calculator, the inputs are the same arbitrary electrical machine geometries as well as the thermal conductivities of the materials used. In addition to these, the thermal calculation tool requires as inputs the coolant thermal properties such as the density, viscosity, and conductivity, the inlet temperature and the flow-rates. Based on the aforesaid inputs, together with the calculated machine losses from the electromagnetic calculator, the thermal calculator estimates the temperatures at various locations within the electrical machine. The cooling technique strongly impacts the power density level [15] and for the purpose of this paper intensive, high flow-rate direct oil-cooling [6] is considered, as described in the following sections since the framework of this research targets high power density.

In order to efficiently extract the heat out of the machine, it is best to locate the heat sink as closely as possible to the heat source. The minimization of the thermal resistances between the heat sources and the coolant enables efficient heat removal [16]–[18]. For the SPM machines under investigation, rectangular cooling channels are thus created in the stator slots, back iron, and teeth, as shown in Fig. 5, where most of the heat generated by the copper and iron losses is located.

Referring to Fig. 5 for the case of the IR topology, oil flows into the flooded stator chamber from the nondrive end of the machine, impinging on the end-winding surfaces through multiple jet-nozzles, as shown by the black arrows. The oil at the nondrive end chamber is forced to flow through the cooling channels in the stator core, and within slots, shown by the white and blue arrows, respectively, in Fig. 5. A thin sleeve is applied in the airgap to ensure that the rotor chamber is free of oil and this helps avoid high windage losses since the machine is running at high speed. A separate oil flow is also added to the machine housing-jacket, as shown by the yellow arrows in the aforesaid figure.

Based on the above cooling concept, a lumped parameter thermal model is developed. For convective heat transfer, the heat transfer coefficients inside the rectangular cooling channels depend on the flow patterns. The flow patterns are in turn determined by the evaluation of the Reynolds number Re, defined as [19]

$$\mathrm{Re} = \frac{U \cdot D_h}{v} \tag{8}$$

where U is the flow velocity in the cooling channel, D_h is the hydraulic diameter, and v is the viscosity of coolant in the cooling channel. The velocity in the cooling channels can be calculated from [16]

$$U = \frac{V}{H \cdot W} \tag{9}$$

where H and W are the height and width of the rectangular cooling channels, respectively, and V is the volume flow rate in each cooling channel.

When the Reynolds number Re of the flow in cooling channel is less than 2300, the flow is said to be laminar, whilst when higher than 2300 the flow in the cooling channels is turbulent. For laminar flow, the heat transfer coefficient h can be calculated from [18]

$$\mathrm{Nu} = \frac{h \cdot D_h}{k_f} = 3.66 + \frac{0.065 \cdot \mathrm{Re} \cdot \mathrm{Pr} \cdot \frac{D_h}{L}}{1 + 0.04(\mathrm{Re} \cdot \mathrm{Pr})^{2/3}} \tag{10}$$

while for turbulent flow [17]

$$\mathrm{Nu} = \frac{h \cdot D_h}{k_f} = 0.023\ \mathrm{Re}^{0.8}\ \mathrm{Pr}^{0.3} \tag{11}$$

where Nu is the Nusselt number which is defined as the ratio of convective to conductive heat transfer of the cooling channel, k_f is thermal conductivity of the cooling fluid, and Pr is the Prandtl number of coolant. From (10) and (11), the heat transfer coefficient at the cooling channels in the slot, tooth, back iron, and machine housing can be determined. For the end winding cooling, the heat transfer coefficient is estimated based on previous experimental work by the authors and measured to be around 1000 to 3000 W/m^{2}K depending on the flow rate and oil jet design [6].

The cooling strategy and procedure for calculating the thermal performance of the OR, DS, and DR topologies follows a similar methodology to that described for the IR, as shown in Fig. 7, with the same color-coding used for the coolant flow arrows as with the IR machine.

VI. Optimization Model

The preceding sections have described the main aspects behind the development of electromagnetic, mechanical, and thermal calculators with defined inputs and outputs for the analysis of any arbitrary SPM machine geometry. The combination of the three domains in a single MATLAB script acts as a multidomain evaluation calculator. This can be readily used within the optimization problem [20], [21], where it is required to maximize the kW/kg considered as the key performance metric for this study.

In order to determine the optimum designs for the different SPM topologies presented, a genetic algorithm which is embedded in the commercial optimization software modeFrontier is used. The optimum machine design is sought in a wide search space defined by the rotor speed and pole pairs which are limited by the maximum fundamental electrical frequency of 1.5 kHz permissible by the power-electronic converter. The optimization model, as shown in Fig. 8, for the case of the IR topology, consists of a so-called "*scheduling project node*" and a "*nested optimization procedure.*" In essential terms, the *scheduling project node* initializes the pole-pairs and speed variables for the nested optimization procedure. For each combination of speed and pole-pair numbers defined in the "*scheduling project node*," the aforesaid parameters are transferred as input parameters to the "*nested optimization procedure*." Continuing with the example of the IR topology, the machine geometry is characterized by seven defining variables, grouped under the heading "Input Variables," shaded in blue in Fig. 7 and related with the geometry presented in Fig. 3. These variables are the split ratio "*k*" stator inner diameter "S_{ID}" aspect ratio "*k_form*" magnet height "M_{height}," tooth width coefficient "$\mathrm{TW}_{\mathrm{coeff}}$" tooth height coefficient "$\mathrm{TH}_{\mathrm{coeff}}$," and carbon fiber sleeve thickness "$\mathrm{SL}_{\mathrm{th}}$." These parameters are easily understandable by the electrical machine designer and allow us to parameterize the main geometry of the machine. The defining input variables and their relation to the machine geometries for each topology shown in Fig. 3 are listed in Table II.

With the range and number of discrete values set for the input variables, the next step is to define the Design of Experiment (DoE), the optimization algorithm, and the multidomain calculation scripts, as shown and shaded in brown in Fig. 8. For the DoE, based on the upper and lower limits together with the number of discrete values for the seven input variables, an initial population of machine designs is generated using a pseudorandom sequence.

The initial population is typically set to around 300. The optimization algorithm is selected to achieve fast computation and solution robustness. The final part in the solver options core is the MATLAB interface block enabling information exchange between the algorithm and the multidomain calculators presented in the previous sections.

This interface enables the optimization to access the electromagnetic-thermal-mechanical model and return the results to the optimization algorithm. This brings the setting-up of the optimization problem to the third and final level, shaded

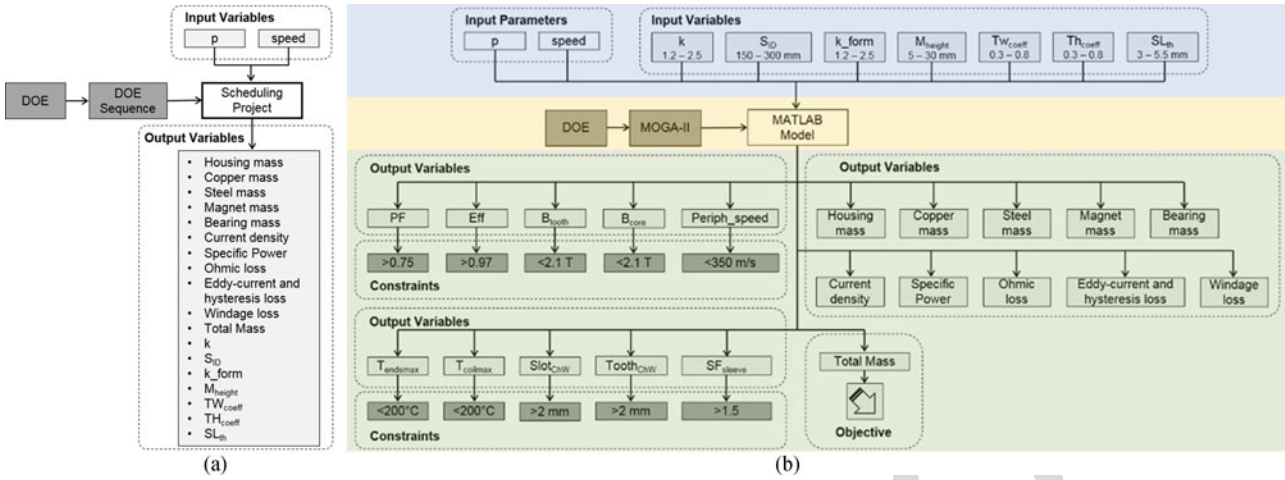

Fig. 8. modeFrontier optimization model for 1 MW IR aerospace machine. (a) *Scheduling project node.* (b) *Nested optimization procedure.*

TABLE II
EXPRESSIONS FOR INPUT VARIABLES

Input variable	IR	OR	DS	DR
k	$\frac{S_{\mathrm{OD}}}{S_{\mathrm{ID}}}$	$\frac{R_{\mathrm{OD}}-2(M_{\mathrm{height}}+AG+RS_{\mathrm{th}})}{S_{\mathrm{ID}}}$	$S_{\mathrm{ODext}}/S_{\mathrm{IDext}}$ [OS] $S_{\mathrm{ODint}}/S_{\mathrm{IDint}}$ [IS]	✗
S_{ID}	S_{ID}	✗	✗	✗
k_form	L_a/S_{ID}	L_a/R_{OD}	L_a/S_{IDext}	L_a/R_{ODext}
M_{height}	M_{height}	✗	✗	✗
$\mathrm{TW}_{\mathrm{coeff}}$	$\frac{6p}{\pi}\frac{T_{\mathrm{width}}}{S_{\mathrm{ID}}}$	$\frac{6p}{\pi}\frac{T_{\mathrm{width}}}{R_{\mathrm{OD}}-2(M_{\mathrm{height}}+AG+RS_{\mathrm{th}})}$	$\frac{6p}{\pi}\frac{T_{\mathrm{width\_ext}}}{S_{\mathrm{IDext}}}$ [OS] $\frac{6p}{\pi}\frac{T_{\mathrm{width\_int}}}{S_{\mathrm{ODint}}}$ [IS]	$\frac{6p}{\pi}\frac{T_{\mathrm{width}}}{R_{\mathrm{OD\_ext}}-2(M_{\mathrm{height\_ext}}+AG_{\mathrm{ext}}+RS_{\mathrm{th\_ext}})}$
$\mathrm{TH}_{\mathrm{coeff}}$	$\frac{2T_{\mathrm{height}}}{S_{\mathrm{OD}}-S_{\mathrm{ID}}}$	$\frac{2T_{\mathrm{height}}}{R_{\mathrm{OD}}-2(M_{\mathrm{height}}+AG+RS_{\mathrm{th}})-S_{\mathrm{ID}}}$	$\frac{2(T_{\mathrm{height\_ext}}-TS_{\mathrm{height\_ext}})}{S_{\mathrm{ODext}}-S_{\mathrm{IDext}}}$ [IS] $\frac{2(T_{\mathrm{height\_int}}-TS_{\mathrm{height\_int}})}{S_{\mathrm{ODint}}-S_{\mathrm{IDint}}}$ [OS]	✗
$\mathrm{SL}_{\mathrm{th}}$	$\mathrm{SL}_{\mathrm{th}}$	✗	✗	✗
$R_{\mathrm{OD\_ext}}$	✗	✗	✗	$R_{\mathrm{OD\_ext}}$
Delta_PM_int	✗	✗	✗	$\frac{M_{\mathrm{height\_int}}}{R_{\mathrm{ID\_int}}/2+M_{\mathrm{height\_int}}}$
Delta_PM_ext	✗	✗	✗	$\frac{M_{\mathrm{height\_ext}}}{R_{\mathrm{OD\_ext}}/2-RS_{\mathrm{th\_ext}}}$
Delta_st	✗	✗	✗	$\frac{S_{\mathrm{height}}}{R_{\mathrm{OD\_ext}}/2-M_{\mathrm{height_{int}}}-RS_{\mathrm{th\_ext}}-AG_{\mathrm{ext}}}$
S_{IDext}	✗	✗	S_{IDext}	✗
overlap_ratio	✗	✗	$2p\alpha/\pi$	✗

in green in Fig. 8, in which the *output variables* and *optimization targets* are defined. The problem in hand is single-objective in nature, targeting the minimization of the machine total mass (active plus nonactive parts). In achieving this target, a number of constraints are defined on the outputs. The first two constraints "T_{endsmax}" and "T_{coilmax}" relate to the thermal limitations, and ensure that for any design to be considered feasible the temperature in the winding must not exceed a defined limit, which for the case in hand is set as 200 °C corresponding to class C insulation. Also related to the thermal domain, minimum practical cooling channel areas are defined by the parameters "$Slot_{\mathrm{ChW}}$" and "$Tooth_{\mathrm{ChW}}$." For a design to be considered feasible the power factor "PF" and the efficiency "eff" must also be higher than defined thresholds (in this case power factor over 0.75 and efficiency over 97%) while the on-load tooth and core flux densities are limited to up to 2.1 T according to the BH characteristics of the chosen material. The final output variable constraints relate to the mechanical domain and impose a peripheral speed "*Periph_speed*" of up to 350 m/s and a rotor factor of safety "SF_{sleeve}" above 1.5.

The optimization has been performed on a PC with Quad Intel Xeon 3.5 GHz CPU, 32 GB of installed RAM and takes around 2 to 2.5 h for the optimization and generation of one design. To generate a topology chart consisting of 25 design points, as shown in Fig. 9, the total time required is around 62 h.

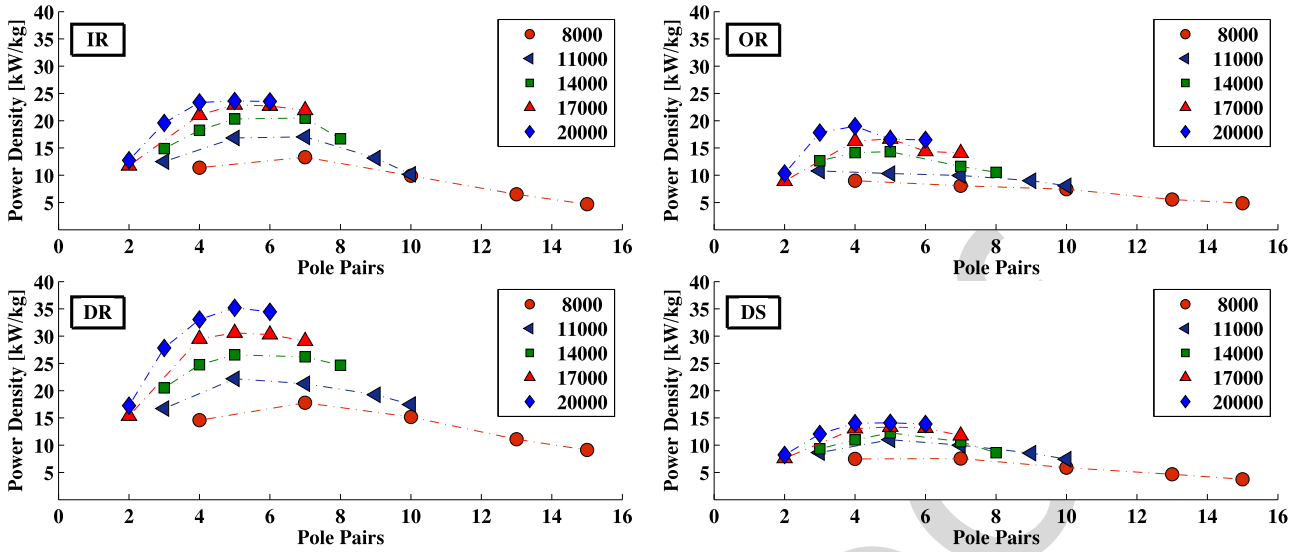

Fig. 9. Power density against pole pair of the machine topologies.

VII. Specific Power Characteristics of 1 MW PM Machines for Aerospace Applications

Using the methodology described in the previous section, the four radial SPM machines are optimized for a range of speeds from 8 to 20 krpm considering different pole numbers corresponding to an upper frequency limit of 1.5 kHz. The machine power was taken equal to 1 MW. The coolant flow rate is 150 L/min with an inlet temperature of 50 °C. Fig. 9 shows the results of the optimization with the power-density (kW/kg) plotted against the number of pole pairs for different rotor speeds.

For a fixed output power, the trend is for the power density to increase with the speed due to multiple factors. The lower torque requirement for increasing speeds leads to a reduced airgap radius and thus a smaller machine size. From the same figure, it is noted that for each speed clearly there is a pole pair number that yields the best power-density. As the pole number (and hence machine frequency increase), the iron mass for a given working flux density reduces, as does the copper loss due to the reduced length of turn, however, the specific iron losses increase due to the higher eddy-currents. The optimum balance between the copper and iron losses is sought by the optimization algorithm and the result depends on the electrical frequency, electrical steel thickness, and the thermal management.

In order to understand the power density and comparative PM topology trends of Fig. 9, it is important to put things in perspective. Focusing deeper on the results of the optimization, the total mass of each design and its segregation into various active and inactive components is presented in Fig. 10. On the same figure, the ratio of the active with respect to the total mass $k_{A/T}$ is plotted on the secondary y-axis. The total mass as well as the active-to-total mass ratio reduce with the increase in the rotor speed. This is mainly caused by the reduction in size due to the lower torque. Significant differences in the distribution of the active and nonactive mass for the different topologies across different speeds can be observed. It can be, therefore, deduced that the power-density achieved when optimizing the active elements only and adding the inactive parts postoptimization, differ to those obtained if the nonactive parts are included within the optimization algorithm, as proposed in this research.

Further important observations can be made when the losses and the maximum machine operational temperature are considered. In Fig. 11, the losses pertaining to the different optimized SPM topologies are segregated. The efficiency limit of 97% imposed by the application translates to a maximum level of admissible losses of 30 kW represented by the dashed red line in the aforesaid figure. It is observed that the iron losses increase with the rotational speed and the number of pole pairs, however, they are always significantly lower than the copper losses. The comparatively high amount of copper losses suggests that the intensive cooling strategy proposed which involves direct slot cooling enables the very high current densities of the order of 25 A/mm^2, which is the main source of power density entitlement.

The maximum temperatures calculated for the different optimized SPM designs are also plotted on the secondary y-axis of Fig. 11. The temperature limit of 200 °C imposed by the class C insulation is represented by the dashed black line on the same figure. It can be noticed that the machines are thermally limited for lower pole numbers due to the lower number of cooling channels within the stator structure, therefore, resulting in a reduced surface for heat transfer. The windage losses are negligible in comparison to the other machine losses.

The optimization results can be analyzed and discussed further considering the data presented in Fig. 12. In this figure, five differently shaped markers (▼, ●, ▲, ◊, ■) represent the limits that the optimization algorithm hits in achieving the highest power-density design for the four investigated SPM topologies. In most cases, the optimization algorithm results in saturated designs with high working flux-densities which represent the electromagnetic limits of the structure indicated by the (▼) B_{sat}

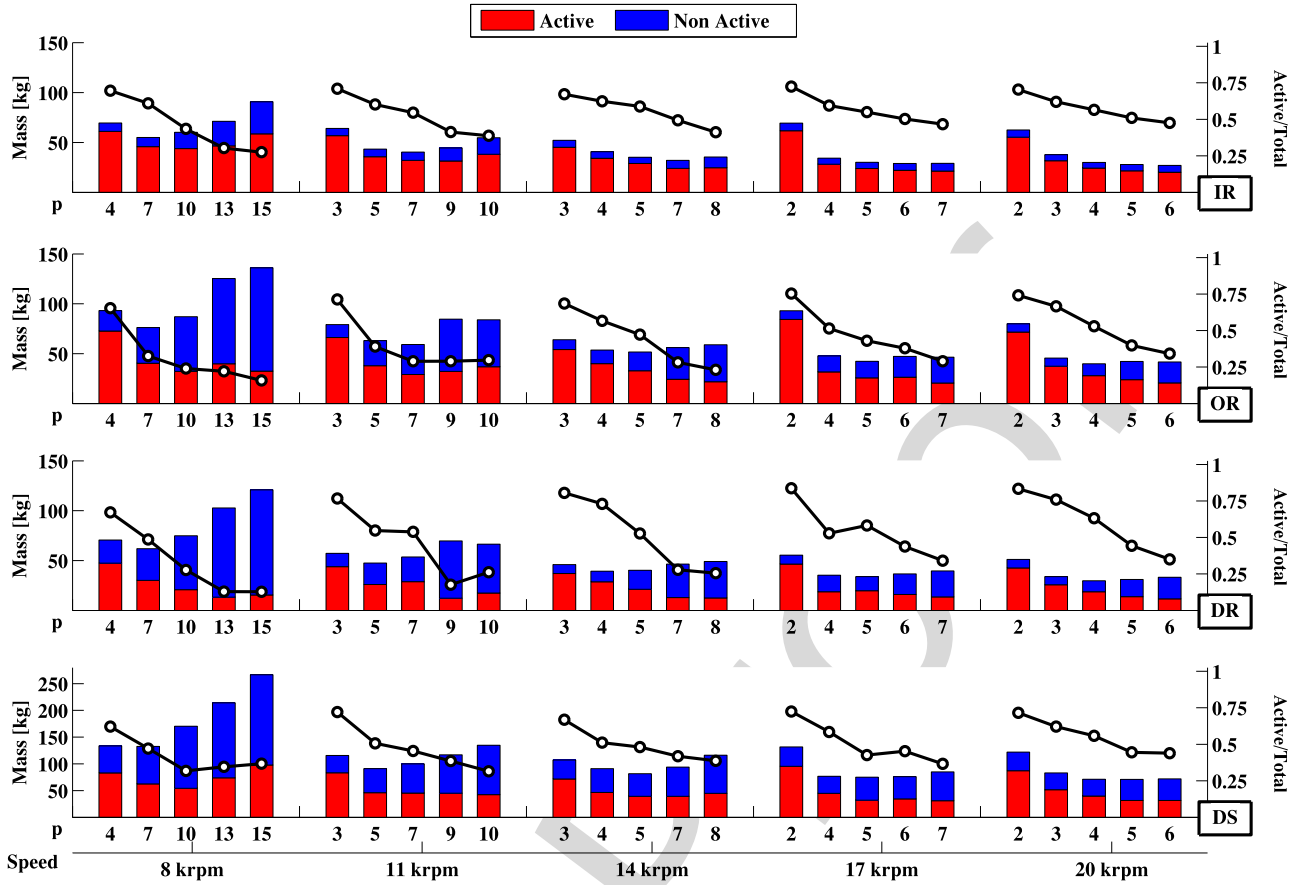

Fig. 10. Mass segregation and $k_{A/T}$ factor against pole pair of the machine topologies investigated.

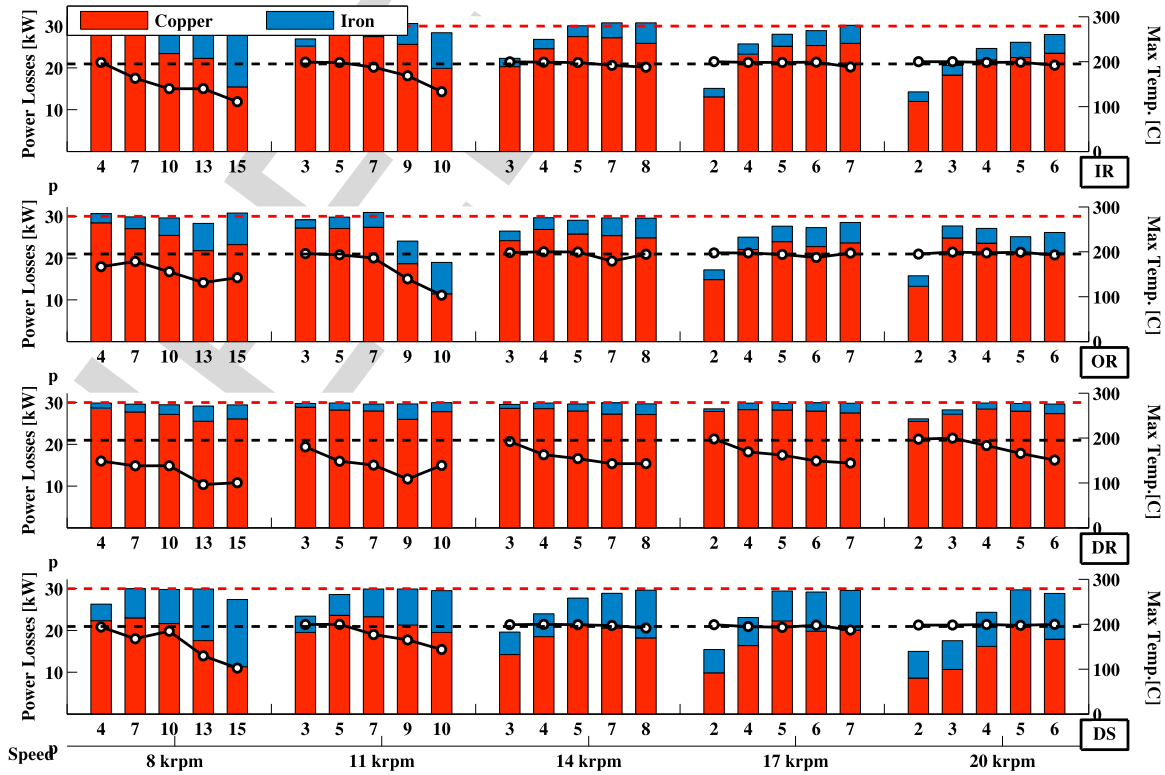

Fig. 11. Loss and maximum temperature distribution against pole pair of the machine topologies investigated.

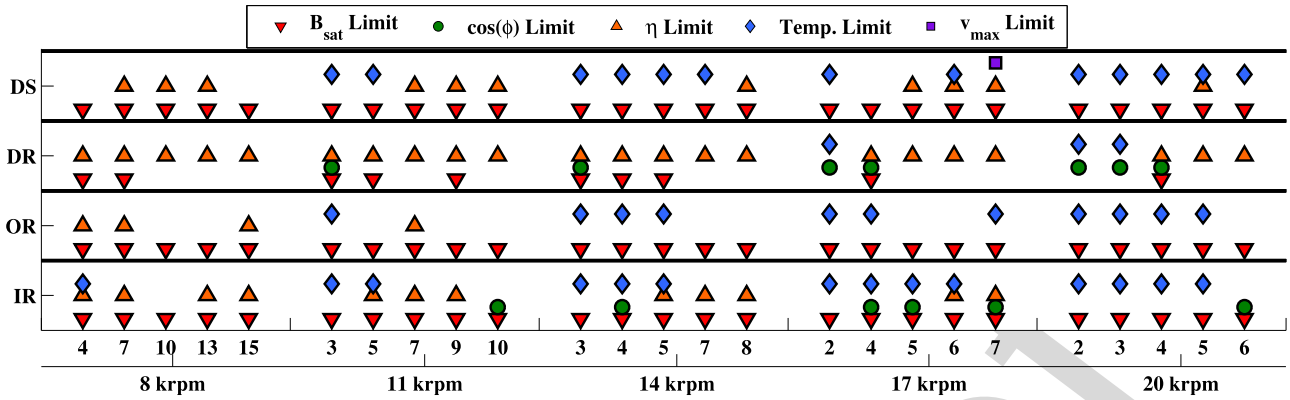

Fig. 12. Limits of the optimized designs for different machine topologies.

limit. Having high working flux-densities in the iron helps in reducing the size and consequently the weight of the machines, however, this also reduces the surfaces for heat extraction. The power factor limit (•), which is set to a minimum value of 0.75, results in being a limiting factor mainly for the DR and IR topologies. Since all designs have a fixed air-gap length, the slot geometry impacts the leakage inductance and thus the power factor plays a role in combination with the flux density saturation limit. Interestingly, the efficiency (▲) and the temperature limits (◊) are distributed in a mutually exclusive way: the designs which are efficiency limited are not in general thermally limited and vice-versa.

For lower speeds, the designs are mainly efficiency limited, while for higher speeds, the designs are primarily thermally limited, as with the reduced volume at high speeds, besides the increase of the power density, the cooling system needs to cater for the increased loss-density, and hence thermal management becomes critical.

Finally from Fig. 12, the mechanical peripheral speed limits (■) are not normally a constraining factor within the optimization except for few cases.

The proposed multidomain optimization tool and methodology enables the investigation of a variety of design combinations and its flexibility is demonstrated by the comparison of different SPM machine topologies in achieving state-of-the-art power densities.

The comparison of the power-density variation with the pole number for the four SPM topologies at 20 krpm is shown in Fig. 13, highlighting the particular suitability of DR topology in achieving the highest power to mass ratio with the defined cooling strategy, materials as well as under no volumetric constraints.The DR topology makes advantage of the double air-gap structure, has no stator back-iron and includes two Halbach arrays that significantly increase the flux density in the active part of the machine. From the same figure, the DR is followed by the IR, OR, and DS configurations in terms of achieving high power densities.

VIII. Tool Validation

The described optimization procedure is implemented on an IR machine requirement specification. Due to size limitations

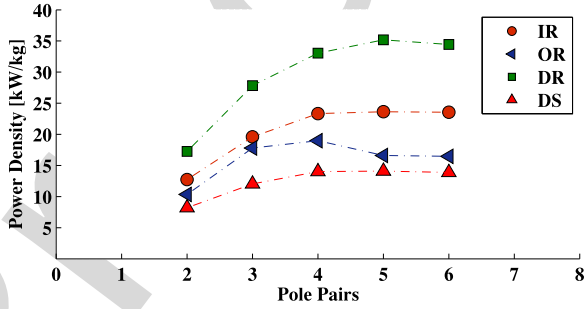

Fig. 13. Comparison machine topology for 20 krpm.

TABLE III
Expressions for Input Variables

Input variable	Range properties
k	1.05–2
S_{ID}	60–150
k_form	0.2–2
$\mathrm{TW}_{\mathrm{coeff}}$	0.3–0.7
$\mathrm{TH}_{\mathrm{coeff}}$	0.3–0.7

and other practical considerations, the machine to be optimized and designed is scaled to a lower power level of 160 kW and higher speed of 32 000 rpm. The machine is still intensively cooled with an oil-flooded stator chamber as that described in Section V, the oil inlet temperature being 120 °C, albeit the flow rate reduced to 15 l/min due to the available system pump rating. Table III lists the variables optimized together with the respective ranges.

The maximum fundamental frequency which the converter can be operated to is 2 kHz, which corresponds to a maximum pole number of 6. Fig. 14 shows the variation of the power-density with pole number, with the dashed red-line representing the maximum converter operational frequency. Taking this frequency limitation into account a 6-pole configuration with a corresponding power density of 7.5 kW/kg is selected for prototyping for the application in hand. Fig. 15 shows the prototyped machine including the lightweight aluminium housing (blue) and the carbon-fibre-wrapped rotor.

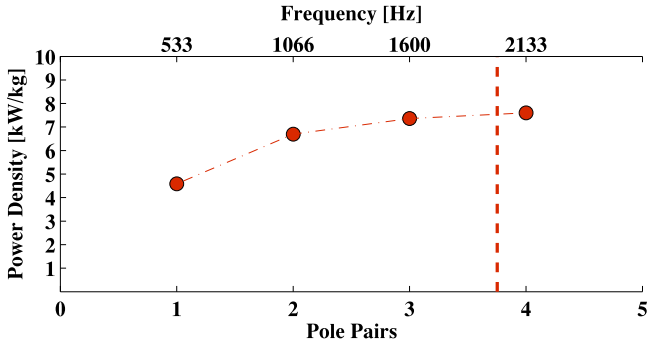

Fig. 14. Variation of power density with pole-number for 160 kW, 32 krpm, with intensive cooling.

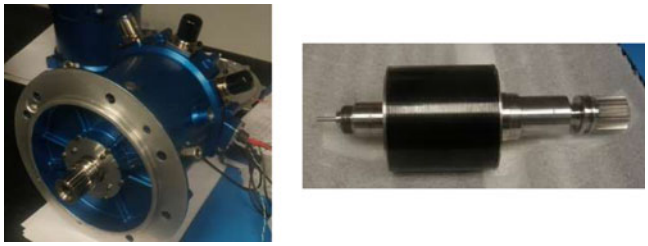

Fig. 15. Prototyped 160 kW, 32 krpm SPM machine, housing (left), rotor (right).

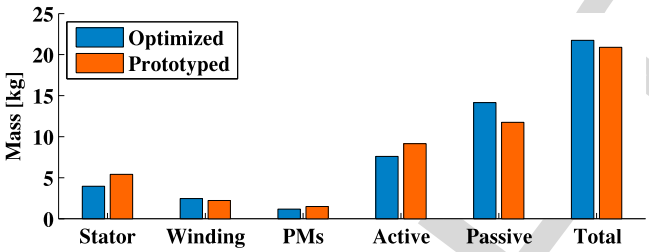

Fig. 16. Comparison of masses as generated from tool, and for final realization of machine design.

The comparison between the masses as optimized with the design software and the actual masses of the realized design (considering further practical manufacturing adjustments) are shown in Fig. 16, highlighting the accuracy of the proposed tool in estimating the nonactive mass.

IX. Conclusion

This paper presented and described the essential building blocks and methodology in developing a rapid tool, which can be used to explore wide search spaces and compare different types of electrical machines at early stages of system integration. For the investigated case, it was shown that 1) very high levels of kW/kg of the order of magnitude claimed in [4] are possible through the described highly intensive cooling strategies together with the integrated optimization of the inactive mass components and 2) the DR topology achieves the highest power density compared to the other radial SPM topologies. While the example and methodology focuses on maximizing the power density kW/kg, a similar integrated multidomain approach can be also readily applied to optimize for other goals typically sought in various industries such as kW/L and $/kg, enabling the system architects to investigate multiple solutions involving electrical machines effectively and take the appropriate system-level decisions.

References

[1] J. M. Miller, Electric Motor R&D., Oak Ridge Nat. Lab., Oak Ridge, TN, USA, Jun. 2013. [Online].Available: https://energy.gov/sites/files/2014/03/f13/ape051_miller_2013_o.pdf
[2] T. Raminosoa *et al.*, "Reduced rare-earth flux-switching machines for traction applications," *IEEE Trans. Ind. Appl.*, vol. 51, no. 4, pp. 2959–2971, Jul. 2015.
[3] A. M. El-Refaie, "Motors/Generators for traction/propulsion applications: A review," *IEEE Trans. Veh. Appl.*, vol. 8, no. 1, pp. 90–99, Jan. 2013.
[4] Siemens AG, Munich, Germany, "World record electric motor for aircraft," Jul 2016.[Online]. Available: www.siemens.com/press/electric-aircraft
[5] D. Gerada, A. Mebarki, N. L. Brown, C. Gerada, A. Cavagnino, and A. Boglietti, "High speed electrical machines—Technologies, trends and developments," *IEEE Trans. Ind. Electron.*, vol. 61, no. 6, pp. 2946–2959, Jun. 2014.
[6] Z. Xu *et al.*, "Mechanical and thermal design of an aeroengine starter/generator," in *Proc. Elect. Mach. Drives Conf.*, May 2015, vol. 1, pp. 1607–1613.
[7] Z. P. Xia, Z. Q. Zhu, and D. Howe, "Analytical magnetic field analysis of halbach magnetized permanent-magnet machines," *IEEE Trans. Magn.*, vol. 40, no. 4, pp. 1864–1872, Jul. 2004.
[8] M. Galea, L. Papini, H. Zhang, C. Gerada, and T. Hamiti, "Demagnetization analysis for halbach array configurations in electrical machines," *IEEE Trans. Magn.*, vol. 51, no. 9, pp. 1–9, Sep. 2015.
[9] D. Golovanov, M. Galea, and C. Gerada, "2D analytical model for dual-stator machines with permanent magnets," in *Proc. IEEE Ind. Elect. Conf.*, Oct. 2016, pp. 1560–1565.
[10] K. J. Binns and P. J. Lawrenson, *Analysis and Computation of Electric and Magnetic Field Problems*. Amsterdam, The Netherlands: Elsevier, 2013.
[11] Y. S. Chen, Z. Q. Zhu, and D. Howe, "Calculation of d- and q-axis inductances of PM brushless ac machines accounting for skew," *IEEE Trans. Magn.*, vol. 41, no. 10, pp. 3940–3942, Oct. 2005.
[12] Z. Q. Zhu, D. Howe, and C. C. Chan, "Improved analytical model for predicting the magnetic field distribution in brushless permanent-magnet machines," *IEEE Trans. Magn.*, vol. 38, no. 1, pp. 229–3238, Aug. 2002.
[13] J. R. Hendershot and T.J.E. Miller, *Design of Brushless Permanent Magnet Motors*. Oxford, U.K.: Magna Phys. Publ., 1994.
[14] High Performance Bearings Catalogue, SKF, Gothenburg, Sweden, 2016. [Online]. Available: http://www.skf.com/group/products/product-tables/index.html.
[15] M. van der Geest, H. Polinder, J. A. Ferreira, and M. Christmann, "Power density limits and design trends of high-speed permanent magnet synchronous machines," *IEEE Trans. Transp. Electrif.*, vol. 1, no. 3, pp. 266–276, Oct. 2015.
[16] M. Popescu, D. A. Staton, A. Boglietti, A. Cavagnino, D. Hawkins, and J. Goss, "Modern heat extraction systems for power traction machines—A Review," *IEEE Trans. Ind. Appl.*, vol. 52, no. 3, pp. 2167–2175, May 2016.
[17] P. M. Lindh *et al.*, "Direct liquid cooling in low-power electrical machines: Proof-of-Concept," *IEEE Trans. Energy Convers.*, vol. 31, no. 4, pp. 1257–1266, Dec. 2016.
[18] S. A. Semiday and J. R. Mayor, "Experimentation of an electric machine technology demonstrator incorporating direct winding heat exchangers," *IEEE Trans. Ind. Electron.*, vol. 61, no. 5, pp. 71–78, Oct. 2014.
[19] Z. Huang and J. Fang, "Multiphysics design and optimization of high-speed permanent-magnet electrical machines for Air blower applications," *IEEE Trans. Ind. Electron.*, vol. 63, no. 5, pp. 2766–2774, May 2016.
[20] Y. Duan and D. Ionel, "A review of recent developments in electrical machine design optimization methods with a permanent-magnet synchronous motor benchmark study" *IEEE Trans. Ind. Appl.*, vol. 49, no. 3, pp. 1269–1275, Nov. 2013.
[21] G. Lei, T. Wang, Y. Guo, J. Zhu, and S. Wang, "System-level design optimization methods for electrical drive systems: Deterministic approach," *IEEE Trans. Ind. Electron.*, vol. 61, no. 12, pp. 6591–6602, Dec. 2014.
[22] T. Wang, F. Wang, H. Bai, and J. Xing, "Optimization design of rotor structure for high speed permanent magnet machines," in *Proc. IEEE Intl. Conf. Elect. Mach. Syst.*, Oct. 2007, pp. 1438–1442.

Dmitry Golovanov received the Ph.D. degree in superconducting electrical machines from Moscow Aviation Institute, Moscow, Russia, in 2011.

He has an experience of working in industry as a Researcher in VNIIEM Corporation JSC, Russia, in the field of design of electrical machines and in Samsung SDI, South Korea, in the field of Li-ion batteries. He is currently a Research Fellow in the University of Nottingham, Nottingham, U.K. His main research interests include high power density electric machines for aerospace and automotive industry application, and superconducting electrical machines.

Luca Papini received the B.S. (Hons.) and M.S. (Hons.) degrees in electrical engineering from the University of Pisa, Pisa, Italy, in 2009 and 2011, respectively. He is currently working toward the Ph.D. degree with the Power Electronic, Motors and Drives Group, University of Nottingham, Nottingham, U.K.

He has been a Visiting Student at the University of Nottingham, developing analytical and numerical models for electrical machines. From June to November 2011, he collaborated with the Department of Energy Engineering, University of Pisa, as a Research Assistant. Since 2013, he has been a Research Assistant with the University of Nottingham. His main research interests include high speed, high power density electric machines, and machine control and levitating system.

David Gerada received the B.Eng. (Hons.) degree in electrical engineering from the University of Malta, Msida, Malta, in 2007, and the Ph.D. degree in high-speed electrical machines from the University of Nottingham, Nottingham, U.K., in 2012.

From 2007 to 2016, he was with the R&D Department at Cummins Generator Technologies, Stamford, U.K., first as an Electrical Machine Design Engineer (2007–2011) and then as a Senior Electrical Machine Design Engineer and Innovation Leader (2011–2016). In 2016, he joined the University of Nottingham as a Senior Research Fellow in Electrical Machines. His research interests include high-speed machines, traction machines, use of novel materials, and multiphysics-based optimization of electrical machines.

Dr. Gerada is a Chartered Engineer in the U.K. and a member of the Institution of Engineering and Technology.

Zeyuan Xu received the Ph.D. degree in mechanical engineering from the University of Manchester, Manchester, U.K., in 2002.

He subsequently worked as a Research Fellow at UMIST, Brunel University, and the University of Nottingham. He is currently a Senior Research Fellow in thermo-mechanical design of high speed electrical machines within the PEMC group at the University of Nottingham, Nottingham, U.K. His main research interests include turbulent thermo-fluid flow, heat transfer enhancement, and thermal management of advanced electrical machines and power electronics.

Chris Gerada (M'05) received the Ph.D. degree in numerical modeling of electrical machines from the University of Nottingham, Nottingham, U.K., in 2005.

He subsequently worked as a Researcher with the University of Nottingham on high-performance electrical drives and on the design and modeling of electromagnetic actuators for aerospace applications. Since 2006, he has been the Project Manager of the GE Aviation Strategic Partnership. In 2008, he was appointed as a Lecturer in the electrical machines; in 2011, as an Associate Professor; and in 2013, as a Professor at the University of Nottingham. His main research interests include the design and modeling of high-performance electric drives and machines.

Prof. Gerada is an Associate Editor for the IEEE TRANSACTIONS ON INDUSTRY APPLICATIONS and is the past Chair of the IEEE IES Electrical Machines Committee.

Multidomain Optimization of High-Power-Density PM Electrical Machines for System Architecture Selection

Dmitry Golovanov, Luca Papini, David Gerada, Zeyuan Xu, and Chris Gerada, *Member, IEEE*

***Abstract*—The power density of electrical machines for transport applications has become a critical aspect and target of optimization. This paper looks at the development of an intelligent, rapid, flexible, and multidomain tool to aid for system-level optimization of electrical machines within next-generation high power density applications. The electromagnetic, thermal, and mechanical aspects are wholly integrated, thus enabling the optimization including the nonactive mass. The implementation and overall architecture of the tool are described, and using a case study drawn from the aerospace industry, the tool is used to compare the power density of various surface permanent magnet topologies including single airgap and dual airgap machines, highlighting the particular suitability of the dual rotor topology in achieving the best power to mass ratio. Finally, the accuracy of the tool is highlighted by practical realization and experimental validation.**

***Index Terms*—High power density, multidomain, optimization, permanent magnet machines, transportation.**

I. Introduction

With the globally increasingly stringent emissions legislations and fuel economy requirements, companies in the transportation sector are actively and intensely researching new technologies, which often involve electrification and hence, the use of electrical machines for either motoring or generation. The performance targets in this type of work are various and depend a lot on the specific industry and application. For example, "high power density" is often a key phrase to distinguish new developments. In the land transportation industry, more specifically for road transportation, where volume is often highly constrained, the key power density metric is the power to volume ratio or kW/L, with numbers such as 4.8 and 4.2 kW/L achieved by Toyota and Nissan [1], respectively. Current hybrid vehicle research programs are targeting in excess of 6 kW/L for the 2020 electrical machine challenge proposed by the U.S. Department of Energy [2], [3]. On the other hand, for the aerospace industry, mass minimization, rather than volume, is critical and the key power density metric is the power to mass ratio or kW/kg, with various numbers published to show achievements of particular developments, such as a recent 5.2 kW/kg by Siemens for a light electric aircraft [4]. Fig. 1 shows two often cited recent developments within the automotive and aerospace industries which present new points of reference for the current state of the art.

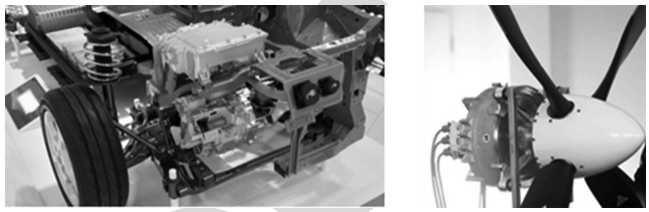

Fig. 1. State-of-the-art high power density motors in the automotive *Nissan* and aerospace industries *Siemens.*

Engineers working on the system concept and integration of the aforementioned more electric transport architectures often face a bottleneck when it comes to the electrical machine. Whilst comprehensive libraries of say, high speed bearings, or high speed turbines are normally available either through supplier input or in-house designs, for the high-performance electrical machines targeted in such work, the available data is very limited. Doing machine sizing in a manual manner for the range of options which the system architects want to investigate is too much time consuming and impractical due to the number of permutations involved, while narrowing down the options risks in missing the system optima altogether. From the foregoing discussion, clearly a tool is required to rapidly generate and assess optimal electrical machine solutions based on defined constraints taking into account the various sciences involved.

This paper describes the development of such a tool. In the first part the methodology, behind the tool development and its implementation are described. The tool is then adopted and used for an aerospace application where it is required to compare the achievable kW/kg for various permanent magnet (PM) machine configurations under an intense cooling regime, with the intent

Manuscript received March 3, 2017; revised June 20, 2017 and September 7, 2017; accepted September 13, 2017. *(Corresponding author: Luca Papini.)*

D. Golovanov, L. Papini, and D. Gerada are with the University of Nottingham, Nottingham NG7 2RD, U.K (e-mail: Dmitry.Golovanov@nottingham.ac.uk; eexlp4@nottingham.ac.uk; david.gerada@nottingham.ac.uk).

Z. Xu is with the Department of Mechanical, University of Nottingham, Nottingham NG7 2RD, U.K (e-mail: Zeyuan.Xu@nottingham.ac.uk).

C. Gerada is with the School of Electrical and Electronic Engineering, University of Nottingham, Nottingham NG7 2RD, U.K (e-mail: chris.gerada@nottingham.ac.uk).

Color versions of one or more of the figures in this paper are available online at http://ieeexplore.ieee.org.

Digital Object Identifier 10.1109/TIE.2017.2772188

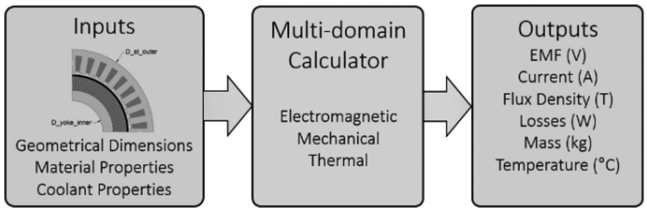

Fig. 2. Multidomain calculators required for optimization.

of establishing, which PM machine topology yields the best power to mass characteristic.

II. Requirement and Methodology

At the early stages of transport electrification projects, the known data with which the system architects start is typically quite limited in nature. This often includes fundamental items, such as the power rating based on the vehicle size, a speed range based on existing turbines or engine designs, together with a list of available coolants. For the example in hand, the power node investigated of 1 MW has to be achieved at a single speed only, and a family of existing turbines within speeds from 8000 to 20 000 rpm are available. While the overall goal of maximizing the kW/kg is known, other items such as the volume, or aspect ratio of the machine are not specified and can be accommodated by the system designers who are often starting from a blank (flexible) design space.

Surface permanent magnet (SPM) machines are known to be capable of achieving the highest power-densities [5] for a single power-speed design point requirement. However, various types of SPM machines exist (inner rotor (IR), outer rotor (OR), dual-airgap, etc.) and it is not immediately obvious which of the aforesaid SPM configurations gives the best kW/kg if the volume is left unconstrained.

Finally, in determining which type of SPM machine yields the best kW/kg, therefore, targeting mass minimization, it is important that the inactive mass is considered within the optimization procedure. By way of example, considering a previously developed high power density aerospace motor, the inactive mass is as high as 34% of the total machine mass [6]. In many classical optimization approaches, the optimization is first done on the electromagnetics, then a housing is designed around the optimized electromagnetic design. However, the housing can be a very significant proportion of the total mass and integrating the housing design with the overall machine kW/kg optimization has high potential for extra power density entitlement.

Appropriate multidomain calculators, which serve as the essential building blocks with which the kW/kg optimization is performed, are required. To this end, for each SPM topology considered, electromagnetic, thermal, and mechanical analytical models are developed, as shown in Fig. 2.

The arbitrary SPM machines are defined in terms of their characterising geometries, constituent materials defined by their magnetic, mechanical and thermal properties, as well as the coolant properties which include the coolant temperature and flow rate. The following sections detail the multidomain calculators implemented and used within the optimization tool.

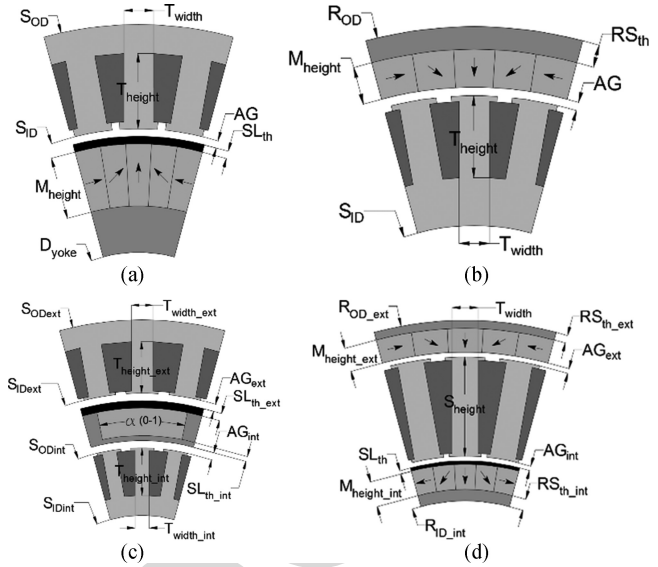

Fig. 3. Considered topologies of PM machines. (a) IR. (b) OR (c) DS. (d) DR.

III. Electromagnetic Calculator

The analytical electromagnetic calculations are performed on any arbitrary geometry defined for the topologies under investigation. The geometrical parameters of the considered machine topologies are shown in Fig. 3, which include single air gap machines, namely the IR and the OR topologies. Furthermore, dual air gap machines are also considered namely the dual stator (DS) and the dual rotor (DR) topologies. An ideal Halbach array structure is selected for the rotor of the IR, OR, and DR topologies, allowing to achieve high fundamental air-gap flux densities whilst reducing the harmonic content [7], and the amount of soft magnetic material required for the rotor core. The electromagnetic model for the considered topologies is for a three-phase single layer distributed winding, with an additional winding group for the (DS) machine. The material selected for the stator structure consists of multiple ultrathin cobalt–iron laminations in a thickness of 0.05 mm which represents a best-in-class material in terms of saturation flux density and high frequency core losses. The arbitrary machine geometry is initially used to compute the no-load magnetic field according to the analytical model of machines with a Halbach array [8]. Under linear behaviour of magnetic materials, the solution for the fundamental of the radial component of flux density in the air gap for the IR and OR topologies is given in [7]. The flux density estimation for the DS topology had been described in [9].

The flux density in the air gaps of the DR machine is evaluated by the introduction of auxiliary virtual PMs [10] that represent the influence of ferromagnetic teeth on the magnetic field. The phase rms value back EMF for the IR, OR, DS, and DR designs is then calculated by the following equation:

$$E_{\rm ph} = \pi\sqrt{2}\, f_e W_{\rm ph} \Phi_0 K_w \tag{1}$$

where $W_{\rm ph}$ is the number of turns per phase, f_e is the electrical fundamental frequency, K_w is the winding factor, and Φ_0 is the no load fundamental flux linkage per pole calculated by the

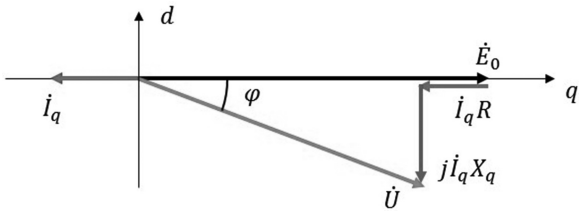

Fig. 4. Vector diagram of considered synchronous machines.

following equation:

$$\Phi_0 = \frac{\pi}{p} L\, R_{\rm st} \left\langle B_r \right\rangle . \tag{2}$$

In the above equation, $\langle B_r \rangle$ is the average value of the fundamental radial flux density component in the air gap, p is the number of rotor pole pairs, L is the active axial length, and $R_{\rm st}$ the radius of the stator surface.

The machine is analyzed in generation mode. The *d*–*q* axis model is adopted with the rotor considered aligned to the *q*-axis. Imposing the *d*-axis current to zero, the resulting phasor diagram is shown in Fig. 4. The phase current $I_{\rm ph}$ can then be estimated from the following equation:

$$\mathrm{I}_{\rm ph} = \frac{P_{\rm el}}{m \cdot E_{\rm ph} \cdot \eta} \tag{3}$$

where $P_{\rm el}$ is the electromagnetic power, m is the number of phases, and η is the efficiency. The number of turns is limited by the fixed dc-link voltage which is set to 2 kV while the winding resistance is calculated considering a slot fill factor of 0.5. The reactance is calculated by means of analytical expressions [11], and the power factor is thus derived accordingly. For the loss calculation, the dc copper losses and the iron losses are considered.

The flux densities for the iron loss calculation are evaluated by means of a linear magnetic circuit calculation and considered as average values on the overall structure. The armature current flux density is evaluated using the approach described in [12].

Given the specific loss of a lamination material say at a frequency of 60 Hz and at an induction of 1 T—$\mathrm{W}_{\mathrm{Fe\_60,1}}$, for any stator fundamental frequency—f_s, and iron flux-density level B_s, the specific iron losses can be approximated from [13] the following equation:

$$W_{\rm Fe} = \frac{W_{\rm Fe\_60,1}}{2} {B_s}^{1.6} \frac{f_s}{60} + \frac{W_{\rm Fe\_60,1}}{2} {B_s}^2 \left(\frac{f_s}{60}\right)^2 \tag{4}$$

where B_s is the on-load flux density [9].

IV. Mechanical Calculator

For the mechanical calculator, the input is the same arbitrary active electrical machine geometry of Fig. 3, together with the mechanical properties of the constituent materials. Based on these inputs, the mechanical calculator estimates the mass of the active materials (i.e., mass of copper, magnets, and iron) and also sizes an appropriate housing around the active geometry with the intent of calculating the nonactive mass. Fig. 5 details the housing sized around the IR SPM configuration showing the axial cross section (*left*) and radial cross section (*right*) with the colour grey denoting the stator housing, colour green denoting the rotor shaft, colour yellow for the stator laminations, colour brown for the copper, and colour red/blue for the permanent magnets.

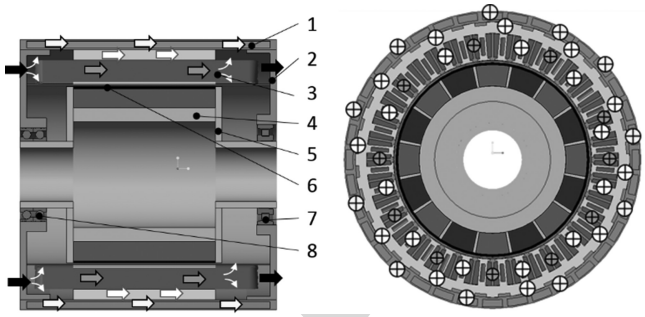

Fig. 5. General housing design and cooling configurations for IR topology.

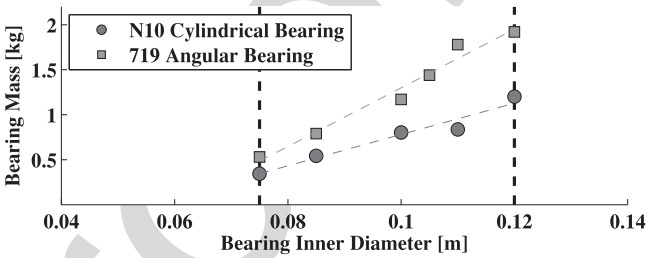

Fig. 6. Bearing mass data and interpolating functions.

TABLE I
Inner Rotor Machine Inactive Parts and Materials

Item#	Descriptions	Material	Density (kg/m^3)	Form
		Stator Housing		
1	Housing shells (inner+outer)	AL6061	2700	Cylindrical shell
2	Two end flanges	AL6061	2700	Hollow disk
3	Cooling channels	AL6061	2700	Rectangular
		Rotor Assembly		
4	Rotor shaft	17-4PH	7780	Cylindrical shaft
5	Rotor balance plates	SS316	7990	Hollow disk
6	Magnet retention sleeve	Carbon Fiber	1600	Cylindrical ring
		Bearings		
7	Drive end bearings		✗	✗
8	Non drive end bearings		✗	✗

Continuing with the case of the IR topology, there are a total of eight inactive parts which are sized for a mechanical factor of safety of at least 1.5 and assuming the machine to be foot mounted. The aforesaid eight inactive parts are numbered in Fig. 5 and listed in Table I. The stator housing (*grey*) is made up of items#1–#3 which correspond to two cylindrical shells (item#1), enclosing end-flanges (item#2), and cooling channels. All the aforesaid components are made of lightweight aluminium having a density of 2700 kg/m^3 in order to minimize the mass.

The rotor assembly supporting the Halbach magnet array is also made up of three constituent parts, items#4–#6 correspond-

ing to a rotor shaft made of high strength, magnetically permeable 17-4ph stainless steel which has a hollow cross section to minimize the mass (item#4), two rotor balance plates made of stainless steel (item#5), and a lightweight carbon-fiber sleeve (item#6) which retains the magnet under compression. Prestress is applied within the carbon-fiber sleeve to ensure that a positive pressure is kept on the magnets throughout the operational speed range as described by the following equation:

$$P_{\text{total}} = P_{\text{prestress}} - P_{\text{mag speed}} - P_{\text{sleeve speed}} > 0 \qquad (5)$$

where $P_{\text{prestress}}$ is the prestress pressure, while $P_{\text{mag speed}}$ $P_{\text{sleeve speed}}$ are the pressure of the magnet and the sleeve, respectively, due to centrifugal affects. The calculation of these depend on the speed, material density as well as the radii of the sleeve and magnet [22]

While ensuring that the condition described by (5) is satisfied, the maximum pressure applied on the sleeve should not result in the stress within the sleeve reaching values beyond the yield strength of the sleeve material as described by the following equation:

$$\sigma_{\text{total}} = \sigma_{\text{prestress}} + \sigma_{\text{sleeve speed}} < \sigma_{\text{material}} \qquad (6)$$

where $\sigma_{\text{prestress}}$ is the stress due to the preload pressure, $\sigma_{\text{sleeve speed}}$ is the sleeve stress at the overspeed condition, and σ_{material} is the material yield strength.

Apart from maintaining the stress of the various components within a safe limit, in sizing the inactive parts it is also important to ensure that there is sufficient torque transmission capability. To this end a minimum shaft diameter $D_{\min}$ is calculated based on the torque transmission requirement as described by the following equation:

$$D_{\min} = \frac{2 \cdot J \cdot \tau}{T} \qquad (7)$$

where T is the shaft torque, and J is the hollow shaft's polar moment of inertia.

With the minimum shaft diameter determined, the bearing inner diameter can, therefore, be selected. For the drive-end, a cylindrical bearing is selected (item#7), while for the nondrive-end a pair of back-to-back angular-contact bearings are used (item#8), as shown in Fig. 5. In determining the bearing mass, linear correlations between bearing inner diameter and mass of the bearing are derived based on the available bearing data [14], as shown in Fig. 6.

The procedure for calculating the inactive mass around arbitrary geometries of the OR, DS, and DR topologies follows a similar methodology to that described for the IR and hence, does not necessitate a detailed description. The cross sections for these machines are shown in Fig. 7 with the same color coding maintained as with the IR machine.

For the OR topology, as shown in Fig. 7(a), the rotor assembly is made-up of a lightweight structure in titanium, with the magnets attached at the inside of the aforesaid structure. Titanium is used for the rotor inactive material since the large rotor diameter would result in a comparatively large inactive mass if stainless steel were to be used as with the IR topology. The DS topology structure is conceptually similar to the OR, with an external stator and stator housing added, as shown in Fig. 7(b). Finally, for the DR topology, the internal rotor assembly has a rigid connection by an end-disk to the external one. The stator core of the machine is supported by bars through the stator laminations which are fixed to a mounting plate at one end of the machine, as shown in Fig. 7(c).

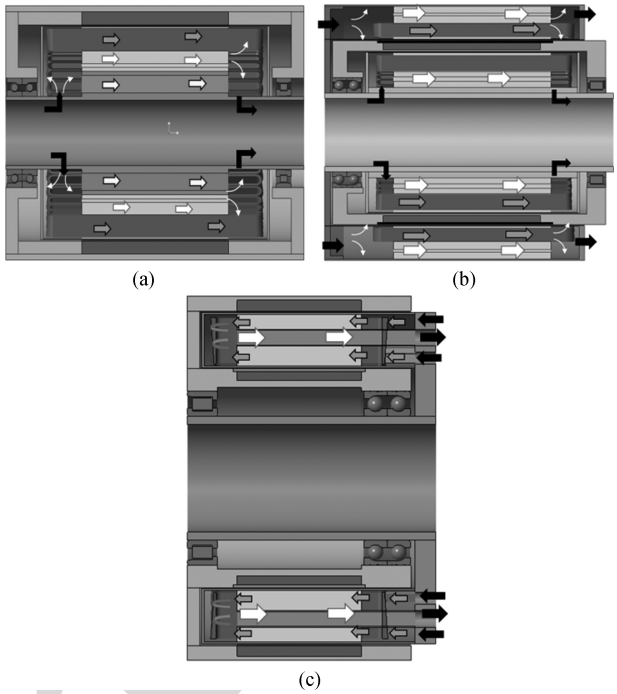

Fig. 7. General housing design and cooling configurations for OR, DS, and DR topologies. (a) Outer rotor machine design. (b) Double stator machine design. (c) Double rotor machine design.

V. Thermal Calculator

For the thermal calculator, the inputs are the same arbitrary electrical machine geometries as well as the thermal conductivities of the materials used. In addition to these, the thermal calculation tool requires as inputs the coolant thermal properties such as the density, viscosity, and conductivity, the inlet temperature and the flow-rates. Based on the aforesaid inputs, together with the calculated machine losses from the electromagnetic calculator, the thermal calculator estimates the temperatures at various locations within the electrical machine. The cooling technique strongly impacts the power density level [15] and for the purpose of this paper intensive, high flow-rate direct oil-cooling [6] is considered, as described in the following sections since the framework of this research targets high power density.

In order to efficiently extract the heat out of the machine, it is best to locate the heat sink as closely as possible to the heat source. The minimization of the thermal resistances between the heat sources and the coolant enables efficient heat removal [16]–[18]. For the SPM machines under investigation, rectangular cooling channels are thus created in the stator slots, back iron, and teeth, as shown in Fig. 5, where most of the heat generated by the copper and iron losses is located.

Referring to Fig. 5 for the case of the IR topology, oil flows into the flooded stator chamber from the nondrive end of the machine, impinging on the end-winding surfaces through multiple jet-nozzles, as shown by the black arrows. The oil at the nondrive end chamber is forced to flow through the cooling channels in the stator core, and within slots, shown by the white and blue arrows, respectively, in Fig. 5. A thin sleeve is applied in the airgap to ensure that the rotor chamber is free of oil and this helps avoid high windage losses since the machine is running at high speed. A separate oil flow is also added to the machine housing-jacket, as shown by the yellow arrows in the aforesaid figure.

Based on the above cooling concept, a lumped parameter thermal model is developed. For convective heat transfer, the heat transfer coefficients inside the rectangular cooling channels depend on the flow patterns. The flow patterns are in turn determined by the evaluation of the Reynolds number Re, defined as [19]

$$\mathrm{Re} = \frac{U \cdot D_h}{v} \tag{8}$$

where U is the flow velocity in the cooling channel, D_h is the hydraulic diameter, and v is the viscosity of coolant in the cooling channel. The velocity in the cooling channels can be calculated from [16]

$$U = \frac{V}{H \cdot W} \tag{9}$$

where H and W are the height and width of the rectangular cooling channels, respectively, and V is the volume flow rate in each cooling channel.

When the Reynolds number Re of the flow in cooling channel is less than 2300, the flow is said to be laminar, whilst when higher than 2300 the flow in the cooling channels is turbulent. For laminar flow, the heat transfer coefficient h can be calculated from [18]

$$\mathrm{Nu} = \frac{h \cdot D_h}{k_f} = 3.66 + \frac{0.065 \cdot \mathrm{Re} \cdot \mathrm{Pr} \cdot \frac{D_h}{L}}{1 + 0.04(\mathrm{Re} \cdot \mathrm{Pr})^{2/3}} \tag{10}$$

while for turbulent flow [17]

$$\mathrm{Nu} = \frac{h \cdot D_h}{k_f} = 0.023\ \mathrm{Re}^{0.8}\ \mathrm{Pr}^{0.3} \tag{11}$$

where Nu is the Nusselt number which is defined as the ratio of convective to conductive heat transfer of the cooling channel, k_f is thermal conductivity of the cooling fluid, and Pr is the Prandtl number of coolant. From (10) and (11), the heat transfer coefficient at the cooling channels in the slot, tooth, back iron, and machine housing can be determined. For the end winding cooling, the heat transfer coefficient is estimated based on previous experimental work by the authors and measured to be around 1000 to 3000 W/m^{2}K depending on the flow rate and oil jet design [6].

The cooling strategy and procedure for calculating the thermal performance of the OR, DS, and DR topologies follows a similar methodology to that described for the IR, as shown in Fig. 7, with the same color-coding used for the coolant flow arrows as with the IR machine.

VI. Optimization Model

The preceding sections have described the main aspects behind the development of electromagnetic, mechanical, and thermal calculators with defined inputs and outputs for the analysis of any arbitrary SPM machine geometry. The combination of the three domains in a single MATLAB script acts as a multidomain evaluation calculator. This can be readily used within the optimization problem [20], [21], where it is required to maximize the kW/kg considered as the key performance metric for this study.

In order to determine the optimum designs for the different SPM topologies presented, a genetic algorithm which is embedded in the commercial optimization software modeFrontier is used. The optimum machine design is sought in a wide search space defined by the rotor speed and pole pairs which are limited by the maximum fundamental electrical frequency of 1.5 kHz permissible by the power-electronic converter. The optimization model, as shown in Fig. 8, for the case of the IR topology, consists of a so-called "*scheduling project node*" and a "*nested optimization procedure.*" In essential terms, the *scheduling project node* initializes the pole-pairs and speed variables for the nested optimization procedure. For each combination of speed and pole-pair numbers defined in the "*scheduling project node*," the aforesaid parameters are transferred as input parameters to the "*nested optimization procedure*." Continuing with the example of the IR topology, the machine geometry is characterized by seven defining variables, grouped under the heading "Input Variables," shaded in blue in Fig. 7 and related with the geometry presented in Fig. 3. These variables are the split ratio "*k*" stator inner diameter "S_{ID}" aspect ratio "*k_form*" magnet height "M_{height}," tooth width coefficient "$\mathrm{TW}_{\mathrm{coeff}}$" tooth height coefficient "$\mathrm{TH}_{\mathrm{coeff}}$," and carbon fiber sleeve thickness "$\mathrm{SL}_{\mathrm{th}}$." These parameters are easily understandable by the electrical machine designer and allow us to parameterize the main geometry of the machine. The defining input variables and their relation to the machine geometries for each topology shown in Fig. 3 are listed in Table II.

With the range and number of discrete values set for the input variables, the next step is to define the Design of Experiment (DoE), the optimization algorithm, and the multidomain calculation scripts, as shown and shaded in brown in Fig. 8. For the DoE, based on the upper and lower limits together with the number of discrete values for the seven input variables, an initial population of machine designs is generated using a pseudorandom sequence.

The initial population is typically set to around 300. The optimization algorithm is selected to achieve fast computation and solution robustness. The final part in the solver options core is the MATLAB interface block enabling information exchange between the algorithm and the multidomain calculators presented in the previous sections.

This interface enables the optimization to access the electromagnetic-thermal-mechanical model and return the results to the optimization algorithm. This brings the setting-up of the optimization problem to the third and final level, shaded

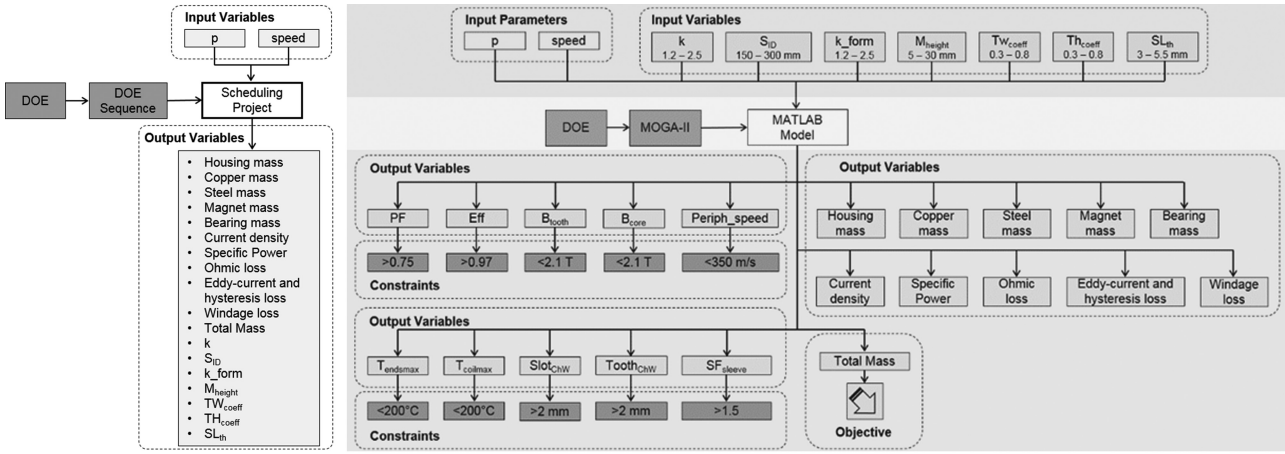

Fig. 8. modeFrontier optimization model for 1 MW IR aerospace machine. (a) *Scheduling project node.* (b) *Nested optimization procedure.*

TABLE II
EXPRESSIONS FOR INPUT VARIABLES

Input variable	IR	OR	DS	DR
k	$\frac{S_{\mathrm{OD}}}{S_{\mathrm{ID}}}$	$\frac{R_{\mathrm{OD}}-2(M_{\mathrm{height}}+AG+RS_{\mathrm{th}})}{S_{\mathrm{ID}}}$	$S_{\mathrm{ODext}}/S_{\mathrm{IDext}}$ [OS] $S_{\mathrm{ODint}}/S_{\mathrm{IDint}}$ [IS]	✗
S_{ID}	S_{ID}	✗	✗	✗
k_form	L_a/S_{ID}	L_a/R_{OD}	L_a/S_{IDext}	L_a/R_{ODext}
M_{height}	M_{height}	✗	✗	✗
$\mathrm{TW}_{\mathrm{coeff}}$	$\frac{6p}{\pi}\frac{T_{\mathrm{width}}}{S_{\mathrm{ID}}}$	$\frac{6p}{\pi}\frac{T_{\mathrm{width}}}{R_{\mathrm{OD}}-2(M_{\mathrm{height}}+AG+RS_{\mathrm{th}})}$	$\frac{6p}{\pi}\frac{T_{\mathrm{width\_ext}}}{S_{\mathrm{IDext}}}$ [OS] $\frac{6p}{\pi}\frac{T_{\mathrm{width\_int}}}{S_{\mathrm{ODint}}}$ [IS]	$\frac{6p}{\pi}\frac{T_{\mathrm{width}}}{R_{\mathrm{OD\_ext}}-2(M_{\mathrm{height\_ext}}+AG_{\mathrm{ext}}+RS_{\mathrm{th\_ext}})}$
$\mathrm{TH}_{\mathrm{coeff}}$	$\frac{2T_{\mathrm{height}}}{S_{\mathrm{OD}}-S_{\mathrm{ID}}}$	$\frac{2T_{\mathrm{height}}}{R_{\mathrm{OD}}-2(M_{\mathrm{height}}+AG+RS_{\mathrm{th}})-S_{\mathrm{ID}}}$	$\frac{2(T_{\mathrm{height\_ext}}-TS_{\mathrm{height\_ext}})}{S_{\mathrm{ODext}}-S_{\mathrm{IDext}}}$ [IS] $\frac{2(T_{\mathrm{height\_int}}-TS_{\mathrm{height\_int}})}{S_{\mathrm{ODint}}-S_{\mathrm{IDint}}}$ [OS]	✗
$\mathrm{SL}_{\mathrm{th}}$	$\mathrm{SL}_{\mathrm{th}}$	✗	✗	✗
$R_{\mathrm{OD\_ext}}$	✗	✗	✗	$R_{\mathrm{OD\_ext}}$
Delta_PM_int	✗	✗	✗	$\frac{M_{\mathrm{height\_int}}}{R_{\mathrm{ID\_int}}/2+M_{\mathrm{height\_int}}}$
Delta_PM_ext	✗	✗	✗	$\frac{M_{\mathrm{height\_ext}}}{R_{\mathrm{OD\_ext}}/2-RS_{\mathrm{th\_ext}}}$
Delta_st	✗	✗	✗	$\frac{S_{\mathrm{height}}}{R_{\mathrm{OD\_ext}}/2-M_{\mathrm{height_{int}}}-RS_{\mathrm{th\_ext}}-AG_{\mathrm{ext}}}$
S_{IDext}	✗	✗	S_{IDext}	✗
overlap_ratio	✗	✗	$2p\alpha/\pi$	✗

in green in Fig. 8, in which the *output variables* and *optimization targets* are defined. The problem in hand is single-objective in nature, targeting the minimization of the machine total mass (active plus nonactive parts). In achieving this target, a number of constraints are defined on the outputs. The first two constraints "T_{endsmax}" and "T_{coilmax}" relate to the thermal limitations, and ensure that for any design to be considered feasible the temperature in the winding must not exceed a defined limit, which for the case in hand is set as 200 °C corresponding to class C insulation. Also related to the thermal domain, minimum practical cooling channel areas are defined by the parameters "$Slot_{\mathrm{ChW}}$" and "$Tooth_{\mathrm{ChW}}$." For a design to be considered feasible the power factor "PF" and the efficiency "eff" must also be higher than defined thresholds (in this case power factor over 0.75 and efficiency over 97%) while the on-load tooth and core flux densities are limited to up to 2.1 T according to the BH characteristics of the chosen material. The final output variable constraints relate to the mechanical domain and impose a peripheral speed "*Periph_speed*" of up to 350 m/s and a rotor factor of safety "SF_{sleeve}" above 1.5.

The optimization has been performed on a PC with Quad Intel Xeon 3.5 GHz CPU, 32 GB of installed RAM and takes around 2 to 2.5 h for the optimization and generation of one design. To generate a topology chart consisting of 25 design points, as shown in Fig. 9, the total time required is around 62 h.

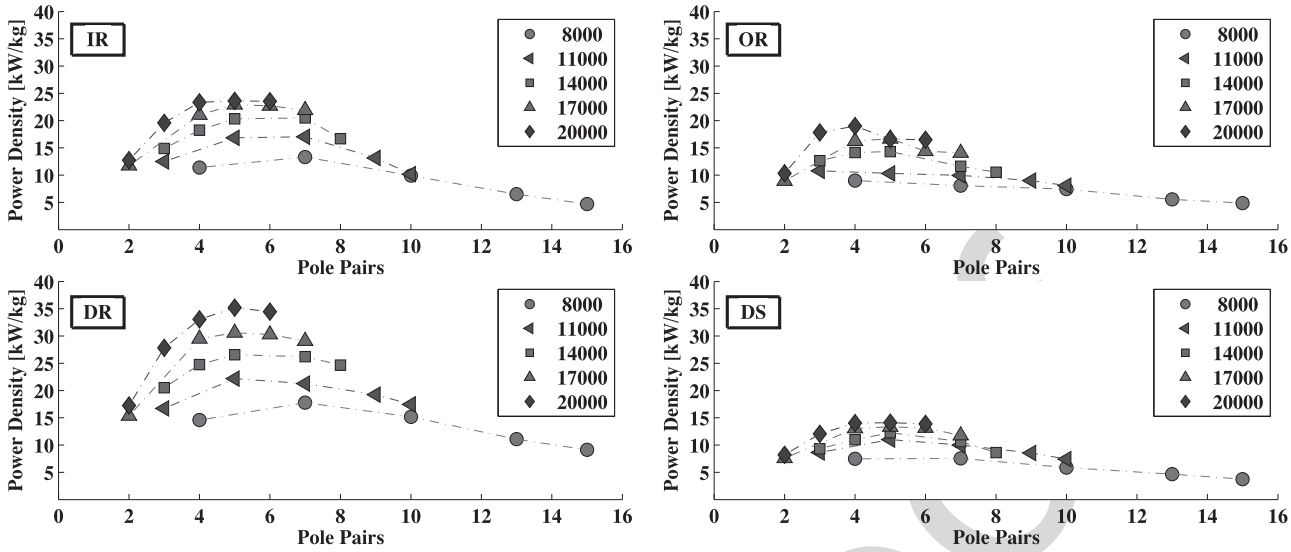

Fig. 9. Power density against pole pair of the machine topologies.

VII. Specific Power Characteristics of 1 MW PM Machines for Aerospace Applications

Using the methodology described in the previous section, the four radial SPM machines are optimized for a range of speeds from 8 to 20 krpm considering different pole numbers corresponding to an upper frequency limit of 1.5 kHz. The machine power was taken equal to 1 MW. The coolant flow rate is 150 L/min with an inlet temperature of 50 °C. Fig. 9 shows the results of the optimization with the power-density (kW/kg) plotted against the number of pole pairs for different rotor speeds.

For a fixed output power, the trend is for the power density to increase with the speed due to multiple factors. The lower torque requirement for increasing speeds leads to a reduced airgap radius and thus a smaller machine size. From the same figure, it is noted that for each speed clearly there is a pole pair number that yields the best power-density. As the pole number (and hence machine frequency increase), the iron mass for a given working flux density reduces, as does the copper loss due to the reduced length of turn, however, the specific iron losses increase due to the higher eddy-currents. The optimum balance between the copper and iron losses is sought by the optimization algorithm and the result depends on the electrical frequency, electrical steel thickness, and the thermal management.

In order to understand the power density and comparative PM topology trends of Fig. 9, it is important to put things in perspective. Focusing deeper on the results of the optimization, the total mass of each design and its segregation into various active and inactive components is presented in Fig. 10. On the same figure, the ratio of the active with respect to the total mass $k_{A/T}$ is plotted on the secondary y-axis. The total mass as well as the active-to-total mass ratio reduce with the increase in the rotor speed. This is mainly caused by the reduction in size due to the lower torque. Significant differences in the distribution of the active and nonactive mass for the different topologies across different speeds can be observed. It can be, therefore, deduced that the power-density achieved when optimizing the active elements only and adding the inactive parts postoptimization, differ to those obtained if the nonactive parts are included within the optimization algorithm, as proposed in this research.

Further important observations can be made when the losses and the maximum machine operational temperature are considered. In Fig. 11, the losses pertaining to the different optimized SPM topologies are segregated. The efficiency limit of 97% imposed by the application translates to a maximum level of admissible losses of 30 kW represented by the dashed red line in the aforesaid figure. It is observed that the iron losses increase with the rotational speed and the number of pole pairs, however, they are always significantly lower than the copper losses. The comparatively high amount of copper losses suggests that the intensive cooling strategy proposed which involves direct slot cooling enables the very high current densities of the order of 25 A/mm^2, which is the main source of power density entitlement.

The maximum temperatures calculated for the different optimized SPM designs are also plotted on the secondary y-axis of Fig. 11. The temperature limit of 200 °C imposed by the class C insulation is represented by the dashed black line on the same figure. It can be noticed that the machines are thermally limited for lower pole numbers due to the lower number of cooling channels within the stator structure, therefore, resulting in a reduced surface for heat transfer. The windage losses are negligible in comparison to the other machine losses.

The optimization results can be analyzed and discussed further considering the data presented in Fig. 12. In this figure, five differently shaped markers $(\blacktriangledown, \bullet, \blacktriangle, \lozenge, \blacksquare)$ represent the limits that the optimization algorithm hits in achieving the highest power-density design for the four investigated SPM topologies. In most cases, the optimization algorithm results in saturated designs with high working flux-densities which represent the electromagnetic limits of the structure indicated by the $(\blacktriangledown)$ B_{sat}

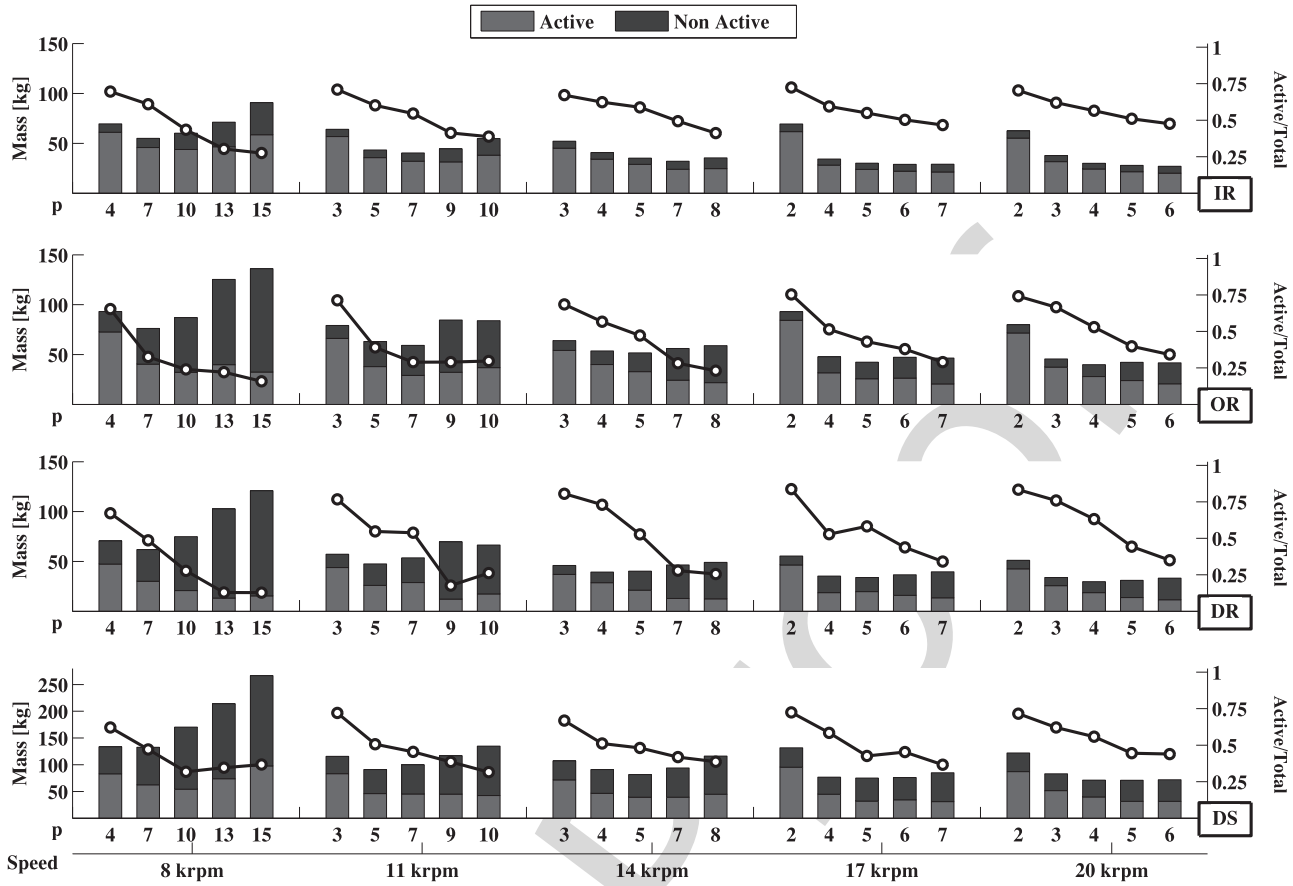

Fig. 10. Mass segregation and $k_{A/T}$ factor against pole pair of the machine topologies investigated.

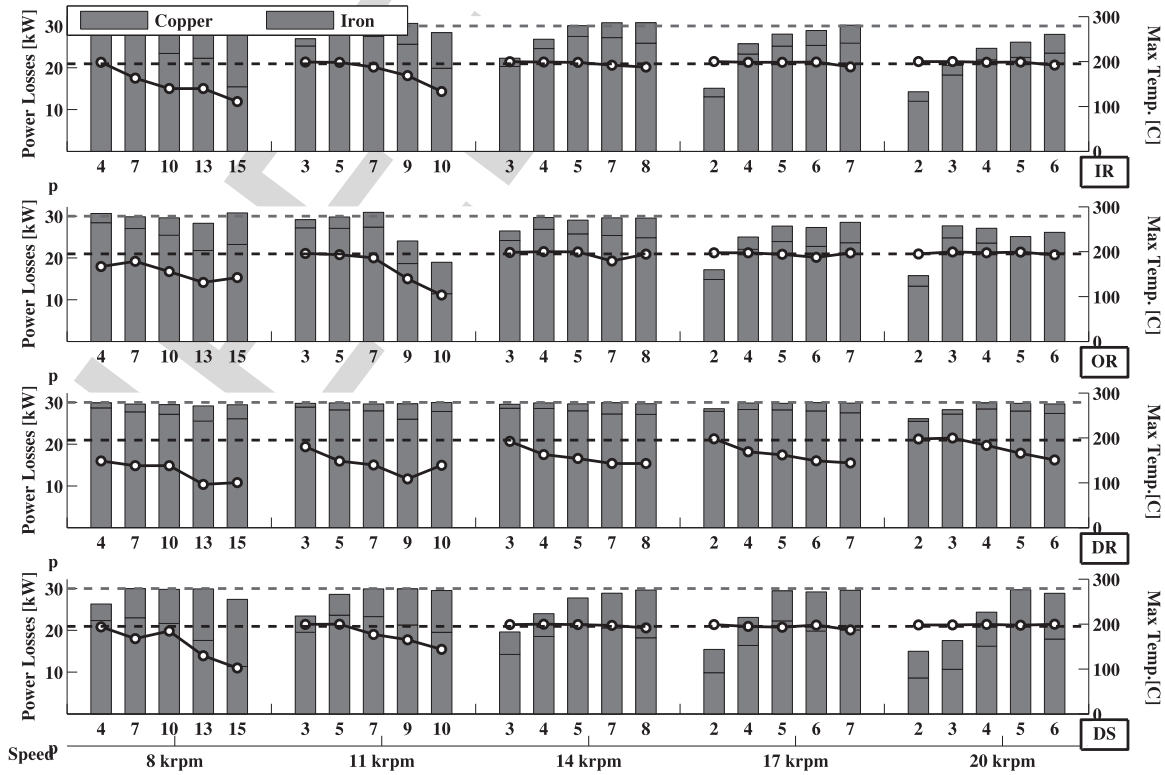

Fig. 11. Loss and maximum temperature distribution against pole pair of the machine topologies investigated.

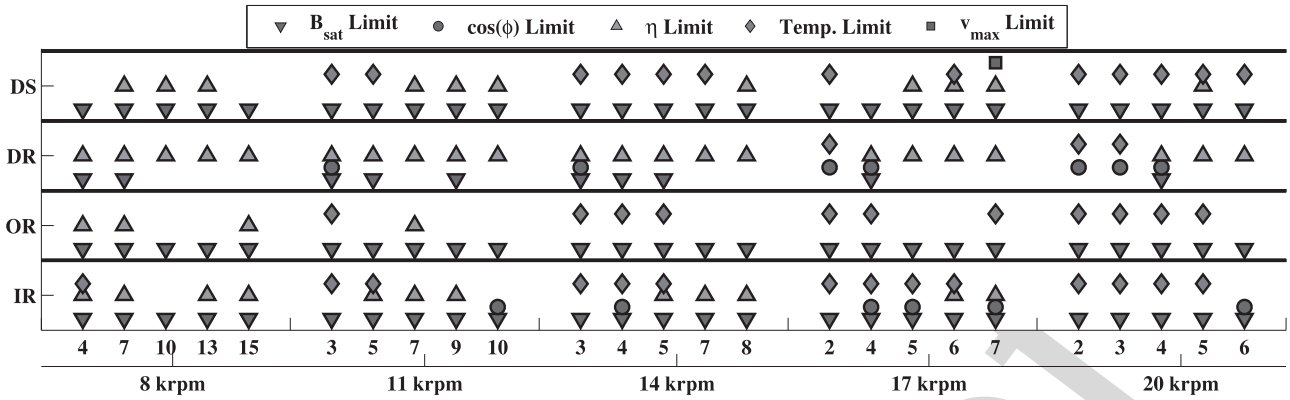

Fig. 12. Limits of the optimized designs for different machine topologies.

limit. Having high working flux-densities in the iron helps in reducing the size and consequently the weight of the machines, however, this also reduces the surfaces for heat extraction. The power factor limit (•), which is set to a minimum value of 0.75, results in being a limiting factor mainly for the DR and IR topologies. Since all designs have a fixed air-gap length, the slot geometry impacts the leakage inductance and thus the power factor plays a role in combination with the flux density saturation limit. Interestingly, the efficiency (▲) and the temperature limits (◊) are distributed in a mutually exclusive way: the designs which are efficiency limited are not in general thermally limited and vice-versa.

For lower speeds, the designs are mainly efficiency limited, while for higher speeds, the designs are primarily thermally limited, as with the reduced volume at high speeds, besides the increase of the power density, the cooling system needs to cater for the increased loss-density, and hence thermal management becomes critical.

Finally from Fig. 12, the mechanical peripheral speed limits (■) are not normally a constraining factor within the optimization except for few cases.

The proposed multidomain optimization tool and methodology enables the investigation of a variety of design combinations and its flexibility is demonstrated by the comparison of different SPM machine topologies in achieving state-of-the-art power densities.

The comparison of the power-density variation with the pole number for the four SPM topologies at 20 krpm is shown in Fig. 13, highlighting the particular suitability of DR topology in achieving the highest power to mass ratio with the defined cooling strategy, materials as well as under no volumetric constraints.The DR topology makes advantage of the double air-gap structure, has no stator back-iron and includes two Halbach arrays that significantly increase the flux density in the active part of the machine. From the same figure, the DR is followed by the IR, OR, and DS configurations in terms of achieving high power densities.

VIII. Tool Validation

The described optimization procedure is implemented on an IR machine requirement specification. Due to size limitations

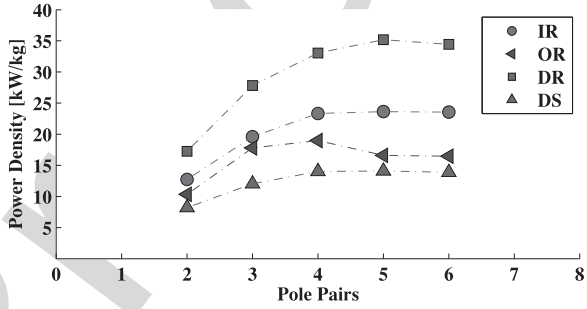

Fig. 13. Comparison machine topology for 20 krpm.

TABLE III
Expressions for Input Variables

Input variable	Range properties
k	1.05–2
S_{ID}	60–150
k_form	0.2–2
$\mathrm{TW}_{\mathrm{coeff}}$	0.3–0.7
$\mathrm{TH}_{\mathrm{coeff}}$	0.3–0.7

and other practical considerations, the machine to be optimized and designed is scaled to a lower power level of 160 kW and higher speed of 32 000 rpm. The machine is still intensively cooled with an oil-flooded stator chamber as that described in Section V, the oil inlet temperature being 120 °C, albeit the flow rate reduced to 15 l/min due to the available system pump rating. Table III lists the variables optimized together with the respective ranges.

The maximum fundamental frequency which the converter can be operated to is 2 kHz, which corresponds to a maximum pole number of 6. Fig. 14 shows the variation of the power-density with pole number, with the dashed red-line representing the maximum converter operational frequency. Taking this frequency limitation into account a 6-pole configuration with a corresponding power density of 7.5 kW/kg is selected for prototyping for the application in hand. Fig. 15 shows the prototyped machine including the lightweight aluminium housing (blue) and the carbon-fibre-wrapped rotor.

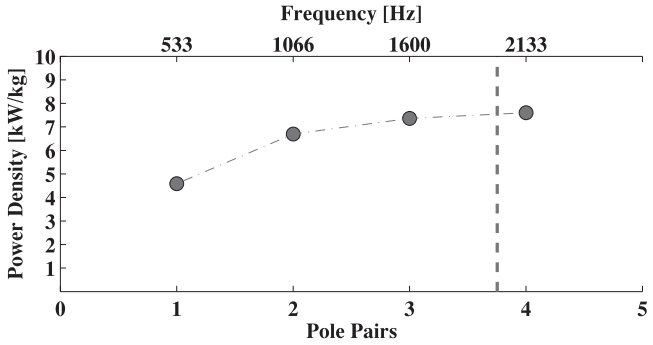

Fig. 14. Variation of power density with pole-number for 160 kW, 32 krpm, with intensive cooling.

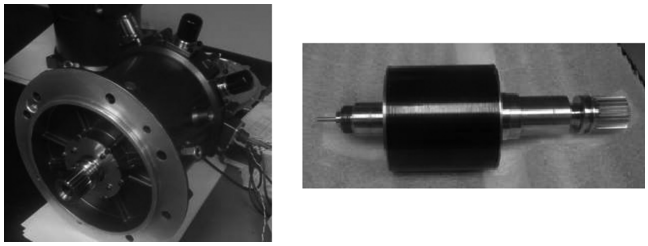

Fig. 15. Prototyped 160 kW, 32 krpm SPM machine, housing (left), rotor (right).

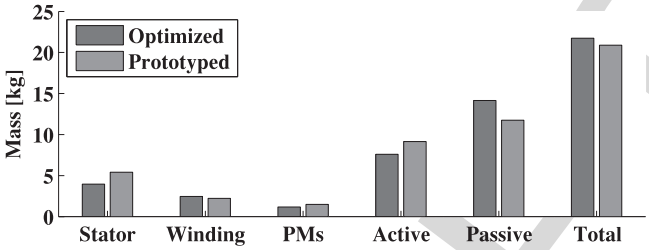

Fig. 16. Comparison of masses as generated from tool, and for final realization of machine design.

The comparison between the masses as optimized with the design software and the actual masses of the realized design (considering further practical manufacturing adjustments) are shown in Fig. 16, highlighting the accuracy of the proposed tool in estimating the nonactive mass.

IX. Conclusion

This paper presented and described the essential building blocks and methodology in developing a rapid tool, which can be used to explore wide search spaces and compare different types of electrical machines at early stages of system integration. For the investigated case, it was shown that 1) very high levels of kW/kg of the order of magnitude claimed in [4] are possible through the described highly intensive cooling strategies together with the integrated optimization of the inactive mass components and 2) the DR topology achieves the highest power density compared to the other radial SPM topologies. While the example and methodology focuses on maximizing the power density kW/kg, a similar integrated multidomain approach can be also readily applied to optimize for other goals typically sought in various industries such as kW/L and $/kg, enabling the system architects to investigate multiple solutions involving electrical machines effectively and take the appropriate system-level decisions.

References

[1] J. M. Miller, Electric Motor R&D., Oak Ridge Nat. Lab., Oak Ridge, TN, USA, Jun. 2013. [Online].Available: https://energy.gov/sites/files/2014/03/f13/ape051_miller_2013_o.pdf

[2] T. Raminosoa *et al.*, "Reduced rare-earth flux-switching machines for traction applications," *IEEE Trans. Ind. Appl.*, vol. 51, no. 4, pp. 2959–2971, Jul. 2015.

[3] A. M. El-Refaie, "Motors/Generators for traction/propulsion applications: A review," *IEEE Trans. Veh. Appl.*, vol. 8, no. 1, pp. 90–99, Jan. 2013.

[4] Siemens AG, Munich, Germany, "World record electric motor for aircraft," Jul 2016.[Online]. Available: www.siemens.com/press/electric-aircraft

[5] D. Gerada, A. Mebarki, N. L. Brown, C. Gerada, A. Cavagnino, and A. Boglietti, "High speed electrical machines—Technologies, trends and developments," *IEEE Trans. Ind. Electron.*, vol. 61, no. 6, pp. 2946–2959, Jun. 2014.

[6] Z. Xu *et al.*, "Mechanical and thermal design of an aeroengine starter/generator," in *Proc. Elect. Mach. Drives Conf.*, May 2015, vol. 1, pp. 1607–1613.

[7] Z. P. Xia, Z. Q. Zhu, and D. Howe, "Analytical magnetic field analysis of halbach magnetized permanent-magnet machines," *IEEE Trans. Magn.*, vol. 40, no. 4, pp. 1864–1872, Jul. 2004.

[8] M. Galea, L. Papini, H. Zhang, C. Gerada, and T. Hamiti, "Demagnetization analysis for halbach array configurations in electrical machines," *IEEE Trans. Magn.*, vol. 51, no. 9, pp. 1–9, Sep. 2015.

[9] D. Golovanov, M. Galea, and C. Gerada, "2D analytical model for dual-stator machines with permanent magnets," in *Proc. IEEE Ind. Elect. Conf.*, Oct. 2016, pp. 1560–1565.

[10] K. J. Binns and P. J. Lawrenson, *Analysis and Computation of Electric and Magnetic Field Problems*. Amsterdam, The Netherlands: Elsevier, 2013.

[11] Y. S. Chen, Z. Q. Zhu, and D. Howe, "Calculation of d- and q-axis inductances of PM brushless ac machines accounting for skew," *IEEE Trans. Magn.*, vol. 41, no. 10, pp. 3940–3942, Oct. 2005.

[12] Z. Q. Zhu, D. Howe, and C. C. Chan, "Improved analytical model for predicting the magnetic field distribution in brushless permanent-magnet machines," *IEEE Trans. Magn.*, vol. 38, no. 1, pp. 229–3238, Aug. 2002.

[13] J. R. Hendershot and T.J.E. Miller, *Design of Brushless Permanent Magnet Motors*. Oxford, U.K.: Magna Phys. Publ., 1994.

[14] High Performance Bearings Catalogue, SKF, Gothenburg, Sweden, 2016. [Online]. Available: http://www.skf.com/group/products/product-tables/index.html.

[15] M. van der Geest, H. Polinder, J. A. Ferreira, and M. Christmann, "Power density limits and design trends of high-speed permanent magnet synchronous machines," *IEEE Trans. Transp. Electrif.*, vol. 1, no. 3, pp. 266–276, Oct. 2015.

[16] M. Popescu, D. A. Staton, A. Boglietti, A. Cavagnino, D. Hawkins, and J. Goss, "Modern heat extraction systems for power traction machines—A Review," *IEEE Trans. Ind. Appl.*, vol. 52, no. 3, pp. 2167–2175, May 2016.

[17] P. M. Lindh *et al.*, "Direct liquid cooling in low-power electrical machines: Proof-of-Concept," *IEEE Trans. Energy Convers.*, vol. 31, no. 4, pp. 1257–1266, Dec. 2016.

[18] S. A. Semiday and J. R. Mayor, "Experimentation of an electric machine technology demonstrator incorporating direct winding heat exchangers," *IEEE Trans. Ind. Electron.*, vol. 61, no. 5, pp. 71–78, Oct. 2014.

[19] Z. Huang and J. Fang, "Multiphysics design and optimization of high-speed permanent-magnet electrical machines for Air blower applications," *IEEE Trans. Ind. Electron.*, vol. 63, no. 5, pp. 2766–2774, May 2016.

[20] Y. Duan and D. Ionel, "A review of recent developments in electrical machine design optimization methods with a permanent-magnet synchronous motor benchmark study" *IEEE Trans. Ind. Appl.*, vol. 49, no. 3, pp. 1269–1275, Nov. 2013.

[21] G. Lei, T. Wang, Y. Guo, J. Zhu, and S. Wang, "System-level design optimization methods for electrical drive systems: Deterministic approach," *IEEE Trans. Ind. Electron.*, vol. 61, no. 12, pp. 6591–6602, Dec. 2014.

[22] T. Wang, F. Wang, H. Bai, and J. Xing, "Optimization design of rotor structure for high speed permanent magnet machines," in *Proc. IEEE Intl. Conf. Elect. Mach. Syst.*, Oct. 2007, pp. 1438–1442.

Dmitry Golovanov received the Ph.D. degree in superconducting electrical machines from Moscow Aviation Institute, Moscow, Russia, in 2011.

He has an experience of working in industry as a Researcher in VNIIEM Corporation JSC, Russia, in the field of design of electrical machines and in Samsung SDI, South Korea, in the field of Li-ion batteries. He is currently a Research Fellow in the University of Nottingham, Nottingham, U.K. His main research interests include high power density electric machines for aerospace and automotive industry application, and superconducting electrical machines.

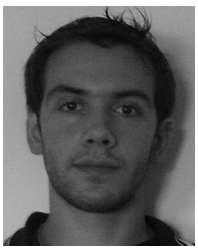

Luca Papini received the B.S. (Hons.) and M.S. (Hons.) degrees in electrical engineering from the University of Pisa, Pisa, Italy, in 2009 and 2011, respectively. He is currently working toward the Ph.D. degree with the Power Electronic, Motors and Drives Group, University of Nottingham, Nottingham, U.K.

He has been a Visiting Student at the University of Nottingham, developing analytical and numerical models for electrical machines. From June to November 2011, he collaborated with the Department of Energy Engineering, University of Pisa, as a Research Assistant. Since 2013, he has been a Research Assistant with the University of Nottingham. His main research interests include high speed, high power density electric machines, and machine control and levitating system.

David Gerada received the B.Eng. (Hons.) degree in electrical engineering from the University of Malta, Msida, Malta, in 2007, and the Ph.D. degree in high-speed electrical machines from the University of Nottingham, Nottingham, U.K., in 2012.

From 2007 to 2016, he was with the R&D Department at Cummins Generator Technologies, Stamford, U.K., first as an Electrical Machine Design Engineer (2007–2011) and then as a Senior Electrical Machine Design Engineer and Innovation Leader (2011–2016). In 2016, he joined the University of Nottingham as a Senior Research Fellow in Electrical Machines. His research interests include high-speed machines, traction machines, use of novel materials, and multiphysics-based optimization of electrical machines.

Dr. Gerada is a Chartered Engineer in the U.K. and a member of the Institution of Engineering and Technology.

Zeyuan Xu received the Ph.D. degree in mechanical engineering from the University of Manchester, Manchester, U.K., in 2002.

He subsequently worked as a Research Fellow at UMIST, Brunel University, and the University of Nottingham. He is currently a Senior Research Fellow in thermo-mechanical design of high speed electrical machines within the PEMC group at the University of Nottingham, Nottingham, U.K. His main research interests include turbulent thermo-fluid flow, heat transfer enhancement, and thermal management of advanced electrical machines and power electronics.

Chris Gerada (M'05) received the Ph.D. degree in numerical modeling of electrical machines from the University of Nottingham, Nottingham, U.K., in 2005.

He subsequently worked as a Researcher with the University of Nottingham on high-performance electrical drives and on the design and modeling of electromagnetic actuators for aerospace applications. Since 2006, he has been the Project Manager of the GE Aviation Strategic Partnership. In 2008, he was appointed as a Lecturer in the electrical machines; in 2011, as an Associate Professor; and in 2013, as a Professor at the University of Nottingham. His main research interests include the design and modeling of high-performance electric drives and machines.

Prof. Gerada is an Associate Editor for the IEEE TRANSACTIONS ON INDUSTRY APPLICATIONS and is the past Chair of the IEEE IES Electrical Machines Committee.